

AMMONIA THERMOMETRY OF STAR FORMING GALAXIES

JEFFREY G. MANGUM

National Radio Astronomy Observatory, 520 Edgemont Road, Charlottesville, VA 22903, USA

JEREMY DARLING

Center for Astrophysics and Space Astronomy, Department of Astrophysical and Planetary Sciences, Box 389, University of Colorado, Boulder, CO 80309-0389, USA

CHRISTIAN HENKEL¹

Max-Planck-Institut für Radioastronomie, Auf dem Hügel 69, 53121 Bonn, Germany

KARL M. MENTEN

Max-Planck-Institut für Radioastronomie, Auf dem Hügel 69, 53121 Bonn, Germany

MEREDITH MACGREGOR²

Harvard University, Department of Astronomy, 60 Garden Street, Cambridge, MA 02138

BRIAN E. SVOBODA^{2,3}

Steward Observatory, University of Arizona, 933 North Cherry Avenue, Tucson, AZ 85721, USA

AND

EVA SCHINNERER

Max-Planck-Institut für Astronomie, Königstuhl 17, 69117 Heidelberg, Germany

Draft version December 3, 2024

ABSTRACT

With a goal toward deriving the physical conditions in external galaxies, we present a study of the ammonia (NH₃) emission and absorption in a sample of star forming systems. Using the unique sensitivities to kinetic temperature afforded by the excitation characteristics of several inversion transitions of NH₃, we have continued our characterization of the dense gas in star forming galaxies by measuring the kinetic temperature in a sample of 23 galaxies and one galaxy offset position selected for their high infrared luminosity. We derive kinetic temperatures toward 13 galaxies, 9 of which possess multiple kinetic temperature and/or velocity components. Eight of these galaxies exhibit kinetic temperatures > 100 K, which are in many cases at least a factor of two larger than kinetic temperatures derived previously. Furthermore, the derived kinetic temperatures in our galaxy sample, which are in many cases at least a factor of two larger than derived dust temperatures, point to a problem with the common assumption that dust and gas kinetic temperatures are equivalent. As previously suggested, the use of dust emission at wavelengths greater than 160 μ m to derive dust temperatures, or dust heating from older stellar populations, may be skewing derived dust temperatures in these galaxies to lower values. We confirm the detection of high-excitation OH ² $\Pi_{3/2}$ J=9/2 absorption toward Arp 220 (Ott et al. 2011). We also report the first detections of non-metastable NH₃ inversion transitions toward external galaxies in the (2,1) (NGC 253, NGC 660, IC 342, and IC 860), (3,1), (3,2), (4,3), (5,4) (all in NGC 660) and (10,9) (Arp 220) transitions.

Subject headings: galaxies: starbursts, ISM: molecules

1. INTRODUCTION

The molecular mass in external galaxies can be well determined by measuring the distribution of Carbon Monoxide (CO) emission (see Young & Scoville 1991). These extragalactic CO measurements have yielded a detailed picture of the molecular mass in many systems. Interpretation of these CO measurements is limited, though, as the emission from the CO molecule is generally dominated by radiative transfer effects, including high optical depth. CO is not a reliable monitor of the spatial density and kinetic temperature in star for-

jmangum@nrao.edu
 jdarling@origins.colorado.edu
 chenkel@mpifr-bonn.mpg.de
 kmenten@mpifr-bonn.mpg.de
 mmacgreg@fas.harvard.edu
 svobodb@email.arizona.edu
 schinner@mpia.de

¹ Also Astronomy Department, Faculty of Science, King Abdulaziz University, P. O. Box 80203, Jeddah, Saudi Arabia

² Also National Radio Astronomy Observatory, 520 Edgemont Road, Charlottesville, VA 22903, USA

³ Also Western Washington University, Department of Physics and Astronomy, 516 High Street, Bellingham, WA 98225-9164

mation regions. Emission line measurements from less-abundant molecules provide a more sensitive diagnostic of the spatial density and kinetic temperature of the dense gas in galaxies (for example, Henkel et al. (1991) for a review, Gao & Solomon (2004a) (HCN), Nguyen et al. (1992) (HCO⁺), Meier & Turner (2005) and Lindberg et al. (2011) (HC₃N), Mauersberger et al. (2003) (NH₃), Mangum et al. (2008, 2013) (H₂CO)).

Results from a survey of a sample of mainly nearby galaxies (Mangum et al. 2008, 2013) have shown that Formaldehyde (H₂CO) is a reliable and accurate density probe for extragalactic environments *where the kinetic temperature is known*. The derivation of n(H₂) in our sample of star forming galaxies relies upon assumed kinetic temperatures. The inversion transitions of NH₃ and the rotational transitions of H₂CO possess very similar excitation conditions, thus likely trace similar dense gas environments. Using the unique sensitivities to kinetic temperature afforded by the excitation characteristics of up to 14 different inversion transitions of NH₃, we have continued our characterization of the dense gas in star forming galaxies by measuring the kinetic temperature in a sample of galaxies selected for their high infrared luminosity. In §2 we discuss the specific properties of the NH₃ molecule which make it a good probe of kinetic temperature. §3 presents our observation summary; §4 our NH₃ measurement results; §5 analyses of our NH₃ measurements, employing Large Velocity Gradient (LVG) model fits. In §6 we discuss our detection of the OH ²Π_{3/2} J=9/2 transition toward Arp 220. In §7 we present an analysis of the remarkable NH₃ absorption spectra measured toward NGC 660. In §9 we study the connection between the high kinetic temperatures derived and models of the heating processes in star forming environments. §11 presents our conclusions.

2. AMMONIA AS A KINETIC TEMPERATURE PROBE

Ammonia (NH₃) is a proven and unbiased tracer of the high density regions within molecular clouds in a variety of galactic and extragalactic environments (see Walmsley & Ungerechts 1983; Mauersberger et al. 2003). Because NH₃ is a symmetric top molecule (energy levels defined by quantum numbers (J,K)), exchange of population between the K-ladders within a given symmetry state (ortho or para) occurs only via collisional processes. The relative intensity of these rotational ground-state inversion transitions for different K-ladders then provides a direct measurement of the kinetic temperature.

The inversion transitions of NH₃ at 23–27 GHz have been used to measure the kinetic temperature in both cool ($T_K \simeq 20$ K) and warm ($T_K \simeq 300$ K) galactic and extragalactic star formation environments. For example, Hermsen et al. (1988) compared measurements of 32 inversion transitions of NH₃ ranging in energy from 23 to 1250 K ((J,K) = (1,1) to (10,8)) toward the Orion-KL star formation region. The wide span of NH₃ excitation afforded by these measurements allowed for a very detailed characterization of the kinetic temperature within the structural components of the Orion-KL star formation environment. A similar study of the NH₃ (1,1) through (9,9) transitions toward NGC 253, IC 342, and Maffei 2 by Mauersberger et al. (2003) revealed warm ($T_K = 100$ –140 K) gas toward NGC 253, IC 342, and

Maffei 2 and cooler gas ($T_K = 60$ K) toward M82. A demonstration of the kinetic temperature sensitivity of the NH₃ transitions is shown in the upper panel of Figure 1. In this demonstration, the (1,1)/(2,2) line ratio monitors the lower kinetic temperatures ($\lesssim 40$ K), while the (2,2)/(4,4) and (5,5)/(7,7) ratios monitor the higher kinetic temperatures ($\lesssim 150$ K and 250 K, respectively).

In addition to the line-intensity comparative measurements of the metastable (J = K) NH₃ inversion transitions which yield kinetic temperature, non-metastable (J≠K) inversion transitions can be used to trace the infrared radiation environment in star formation regions. As originally noted by Morris et al. (1973), for n(H₂) $\lesssim 10^7$ cm⁻³ and no nearby source of infrared radiation the excitation temperatures of the non-metastable transitions remain very low. This low excitation temperature is due to the rapid spontaneous decay from the (J+1,J) states into the (J,J) states ($A_{ij} \sim 0.013$ s⁻¹ for the (2,1)–(1,1) rotational transition). In the presence of a source of infrared flux, Morris et al. (1973) showed that the level populations of the (2,1) and (3,2) non-metastable inversion transitions become inverted. This behavior also holds true for the other non-metastable NH₃ transitions. This sensitivity to background infrared radiation makes the (2,1) transition a sensitive probe of the radiation environment within star formation regions. Figure 1 (bottom) shows the LVG-model predicted excitation temperature of the (2,1) transition within typical physical conditions for our star forming galaxy sample (assuming no background continuum). When an infrared radiation field is introduced the excitation temperature becomes negative (i.e. masing) for n(H₂) $\lesssim 10^5$ cm⁻³, leading to emission in the (2,1) transition.

3. OBSERVATIONS

The measurements reported here were made using the National Radio Astronomy Observatory (NRAO⁴) Green Bank Telescope (GBT) during thirty-four observing sessions from 2009/03/18 through 2012/03/04. Single-pointing measurements were obtained of the NH₃ transitions listed in frequency setup “A50” of Table 1 toward a sample of 23 infrared-luminous and/or star forming galaxies (Table 2) which exhibit H₂CO emission or absorption (Mangum et al. 2008, 2013). Additional measurements of the generally higher-excitation and ortho-NH₃ transitions listed in the other frequency setups described in Table 1 were made toward NGC 253, NGC 660, IC 342, NGC 3079, IC 860, and Arp 220. For galaxies with expected large linewidths (IR 01418+1651, IR 15107+0724, and Arp 220) we used the 200 MHz bandwidth configurations listed in Table 1. Table 2 lists the observation frequency setup(s) used for each galaxy.

All measurements utilized the dual-beam nodding ($\theta_B = 30''$ with beam separation = 179'') technique afforded by the dual- and multi-beam dual-polarization K-band receiver systems at the GBT. Measurements made before 2011/10/23 used the facility dual-beam dual-polarization receiver system, while those made thereafter used beams 2 and 3 of the 7-channel K-band Focal Plane Array (KFPA). Spectra were produced from these

⁴ The National Radio Astronomy Observatory is a facility of the National Science Foundation operated under cooperative agreement by Associated Universities, Inc.

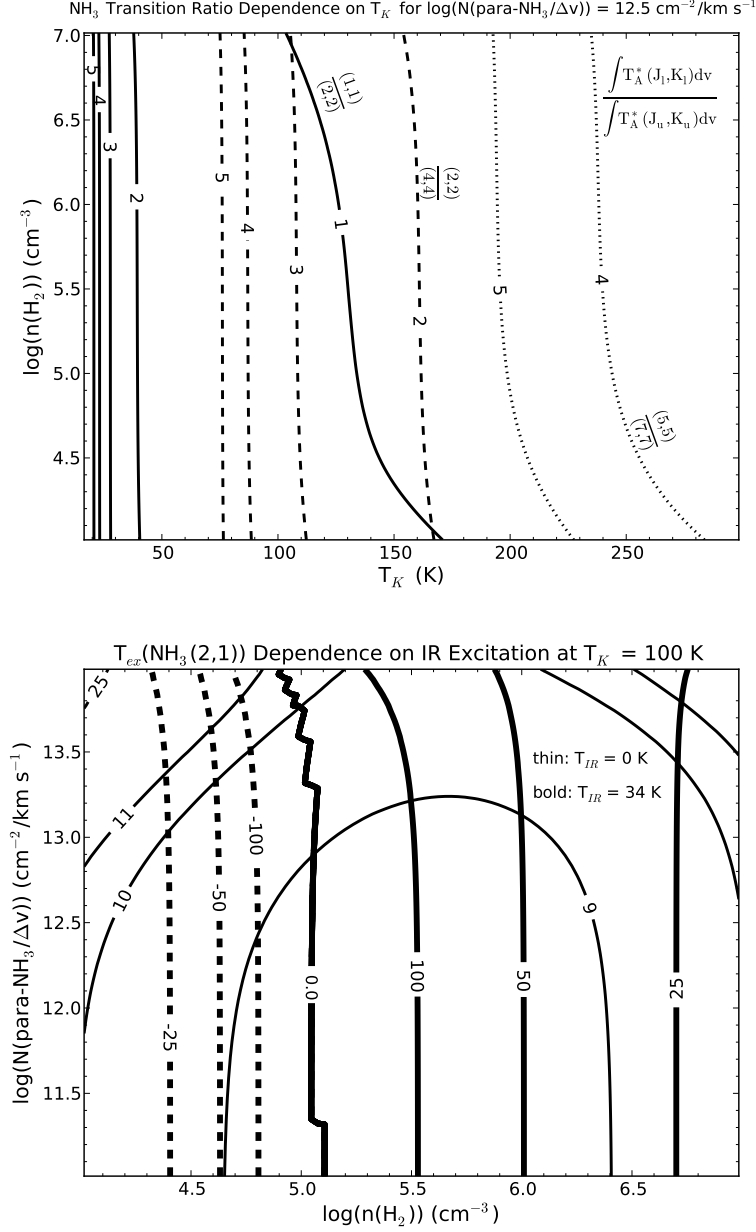


FIG. 1.— *Top*: Example LVG-modelled kinetic temperature sensitivity for the NH₃ (1,1)/(2,2) (solid contours), (2,2)/(4,4) (dashed contours), and (5,5)/(7,7) (dotted contours) transition ratios. Note how the lower-excitation (1,1)/(2,2) ratio is linear with kinetic temperature up to $\sim 40 \text{ K}$, while the higher-excitation (2,2)/(4,4) and (5,5)/(7,7) ratios are relatively linear up to ~ 150 and $\sim 250 \text{ K}$, respectively. *Bottom*: Example LVG-modelled NH₃ (2,1) excitation temperature as a function of spatial density and para-NH₃ column density per unit linewidth at $T_K = 100 \text{ K}$. Thin contours indicate T_{ex} for no infrared radiation field, while bold contours indicate T_{ex} when $T_{\text{IR}} = 34 \text{ K}$ (appropriate for NGC 253 and IC 342; see §5.3). For $n(\text{H}_2) \lesssim 10^5$ the (2,1) transition is inverted (i.e. masing) when subjected to a strong infrared radiation field.

measurements using the GBT spectrometer configured to yield simultaneous measurement of 4 (frequency setups A50, B50, J50, and I50) or 2 (all other frequency setups) spectral windows each with 50 or 200 MHz of bandwidth sampled by 4096 channels. This correlator configuration produced a spectral channel width of 12.2 and 48.8 kHz (0.16 and 0.62 km s^{-1} at 23.7 GHz).

To calibrate all of our measurements to a uniform intensity scale we used the following measurements:

- One or more of the standard flux calibration sources 0137+331 (3C 48), 0139+413 (3C 84),

1331+305 (3C 286) were measured during each observing run.

- An estimate of the atmospheric opacity during each of our observing runs was derived based on atmospheric model calculations using ambient pressure, temperature, and relative humidity measurements. At 23 GHz we found that the zenith opacity $\tau_0 \sim 0.04 - 0.10$ during our observations. Assuming elevation $\gtrsim 30$ degrees implies that the opacity correction to our measured amplitudes is $\lesssim 1.22$.

Combined with a calculation of the aperture efficiency

TABLE 1
MEASURED TRANSITION PROPERTIES AND OBSERVING CONFIGURATIONS

Transition	Frequency (MHz)	E_{upper} (K)	Frequency Setup ^a
NH ₃ (3,1)	22234.5630	167.3	J50
NH ₃ (5,4)	22653.0720	344.5	J50
NH ₃ (4,3)	22688.3490	239.0	J50
NH ₃ (3,2)	22834.1820	151.3	J50
NH ₃ (2,1)	23098.8190	80.0	A50
NH ₃ (1,1)	23694.4955	22.7	A50,C200
NH ₃ (2,2)	23722.6333	63.9	A50,C200
OH ² Π _{3/2} J=9/2 F=4 – 4	23817.6153	512.1	D200
OH ² Π _{3/2} J=9/2 F=5 – 5	23826.6211	512.1	D200
NH ₃ (3,3)	23870.1292	123.1	B50,D200
NH ₃ (4,4)	24139.4163	200.1	A50,C200
NH ₃ (10,9)	24205.2870	1137.6	C200
NH ₃ (5,5)	24532.9887	295.0	B50,E200
NH ₃ (6,6)	25056.0250	407.8	B50,D200,G200
NH ₃ (7,7)	25715.1820	538.3	B50,E200,F200,I50
NH ₃ (8,8)	26518.9810	687.7	F200,G200,H200,I50
NH ₃ (9,9)	27477.9430	853.1	H200,I50
HC ₃ N 3 – 2	27294.2950	2.6	I50

^a Nomenclature: Letter designates a specific spectrometer configuration which includes the associated transitions for a given bandwidth. For example, “A50” for the spectrometer configuration that includes the NH₃ (2,1), (1,1), (2,2), and (4,4) transitions measured using a 50 MHz bandwidth.

TABLE 2
EXTRAGALACTIC AMMONIA TARGET LIST

Source	α (J2000)	δ (J2000)	v_{hel}^a (km s ⁻¹)	D_L^b (Mpc)	T_{dust}^c (K)	L_{IR}^d ($\times 10^{10} L_\odot$)	Obs Frequency Setups ^e
NGC 253	00:47:33.1	-25:17:18	251	3.44 ± 0.24	34	3.41 ± 0.24	A,B,I, and J50
NGC 598	01:33:54.0	+30:40:07	-179	0.88 ± 0.28	...	0.13 ± 0.05	A50
NGC 660	01:43:01.7	+13:38:36	856	12.2 ± 0.9	37	3.03 ± 0.22	A,B, and J50
IR 01418+1651	01:44:30.5	+17:06:09	8101	109.7 ± 7.7	...	36.33 ± 2.72	C200
NGC 891	02:22:33.4	+42:20:57	529	9.43 ± 0.66	28	2.25 ± 0.16	A50
Maffei 2	02:41:55.1	+59:36:15	-17	3.11 ± 0.23	...	0.31 ± 0.05	A50
NGC 1144	02:55:12.2	-00:11:01	8750	115.3 ± 8.1	32	23.86 ± 2.16	A50,C200
NGC 1365	03:33:36.4	-36:08:25	1652	21.5 ± 1.5	32	14.31 ± 1.00	A50
IC 342	03:46:49.7	+68:05:45	31	3.82 ± 0.27	30	1.01 ± 0.07	A50,B50
NGC 2146	06:18:37.7	+78:21:25	918	16.7 ± 1.2	38	12.56 ± 1.36	A50
M 82	09:55:52.2	+69:40:47	203	5.92 ± 0.42	45	15.69 ± 1.11	A50
M 82SW	09:55:50.0	+69:40:43	203	15.69 ± 1.11	A50
NGC 3079	10:01:57.8	+55:40:47	1150	20.7 ± 1.5	32	6.93 ± 0.50	A,B,I, and J50, D200
NGC 3628	11:20:17.2	+13:35:20	847	8.5 ± 0.6	30	1.27 ± 0.09	A50
NGC 3690	11:28:32.2	+58:33:44	3121	48.5 ± 3.4	...	76.96 ± 5.40	A50
NGC 4214	12:15:39.2	+36:19:37	291	3.75 ± 0.27	...	0.07 ± 0.005	A50
NGC 4418	12:26:54.6	-00:52:39	2040	34.7 ± 2.4	...	14.08 ± 0.98	A50
Mrk 231	12:56:14.2	+56:52:25	12642	178.1 ± 12.5	...	319.46 ± 22.45	A50
IC 860	13:15:04.1	+24:37:01	3866	53.8 ± 3.8	...	11.95 ± 0.93	A50,B50
M 83	13:37:00.9	-29:51:57	518	4.03 ± 0.28	31	1.57 ± 0.11	A50
IR 15107+0724	15:13:13.1	+07:13:27	3897	61.9 ± 4.4	...	19.98 ± 1.44	C200
Arp 220	15:34:57.1	+23:30:11	5434	82.9 ± 5.8	44	167.11 ± 11.70	C,D,E,F,G, and H200
NGC 6946	20:34:52.3	+60:09:14	48	5.49 ± 0.39	30	1.51 ± 0.11	A50
NGC 6951	20:37:14.1	+66:06:20	1425	24.3 ± 1.7	...	3.74 ± 0.26	A50

^a Heliocentric velocity drawn from the literature.

^b NED Hubble flow distance corrected for Virgo cluster, Great Attractor, and Shapley supercluster. For NGC 598 no Hubble flow distance was available, so NED “redshift-independent” distance assumed.

^c From Gao & Solomon (2004b), who used IRAS 60 and 100 μ m dust continuum emission ratios with an assumed dust emissivity $\propto \nu^{-\beta}$ with $\beta = 1.5$.

^d Luminosities from Sanders et al. (2003), derived from IRAS fluxes over 8 to 1000 μ m.

^e See Table 1 for transitions measured.

using the following GBT-recommended formula:

$$\eta_A = 0.72 \exp \left[-(\alpha \nu (GHz))^2 \right] \quad (1)$$

where $\alpha = 0.0163$ for measurements made on or before 2009/02/06, while $\alpha = 0.0145$ for measurements made after 2009/02/06. The conversion between antenna temperature corrected for atmospheric attenuation (T_A^*) and flux density (S) was calculated using:

$$\frac{T_A^*}{S} = 2.846 \eta_A \exp(-\tau_0 \csc(EL)) \text{ K/Jy} \quad (2)$$

Fluxes for our calibrator sources were calculated using the measurements and frequency-dependent relations derived by Ott et al. (1994). The T_A^*/S values for our thirty-four observing sessions which comprise our NH_3 measurements ranged from 0.91 ± 0.07 K/Jy to 1.92 ± 0.07 K/Jy. With a calculated value for T_A^*/S appropriate for the measurements made in each observing run we then normalized all of our NH_3 measurements to a common T_A^*/S value of 1.88 K/Jy, thus allowing us to average spectra for a given galaxy over multiple observing runs. This calibration sequence assumes point-source emission. To calibrate to a main beam brightness temperature scale, one can use $\eta_{mb} \simeq 1.32 \eta_A$ with brightness temperature defined as $T_{mb} \simeq \frac{T_A^*}{\eta_{mb}}$. GBT amplitude calibration is reported to be accurate to 10-15% at all frequencies, limited mainly by temporal drifts in the noise diodes used as amplitude calibration standards.

4. RESULTS

In the following all spectra have been smoothed to either 5 or 10 km s^{-1} to increase the signal-to-noise ratio of individual channels in these measurements. Table 3 lists the peak intensity, velocity, line width, and integrated intensity derived from both direct channel-by-channel integration of the FWZI line profiles and Gaussian fits for those galaxies with detected NH_3 emission or absorption. The measured band-center continuum level derived from the zero-level offset of our spectroscopic measurements is also listed. Spectra for the detected galaxies are displayed in Figures 2 through 10. These spectra include the first detections of non-metastable NH_3 inversion transitions toward external galaxies in the (2,1) (NGC 253, NGC 660, IC 342, and IC 860), (3,1), (3,2), (4,3), (5,4) (all in NGC 660) and (10,9) (Arp 220) transitions.

5. ANALYSIS

5.1. Kinetic Temperature Derivation Using LVG Models

To derive the kinetic temperature of the dense gas in our galaxy sample, we use a model which incorporates the Large Velocity Gradient (LVG) approximation (Sobolev 1960) to the radiative transfer. The detailed properties of our implementation of the LVG approximation are described in Mangum & Wootten (1993). This simplified solution to the radiative transfer equation allows for a calculation of the global dense gas properties in a range of environments. As noted by Mangum & Wootten (1993), one of the major sources of uncertainty in an LVG model prediction of the physical conditions

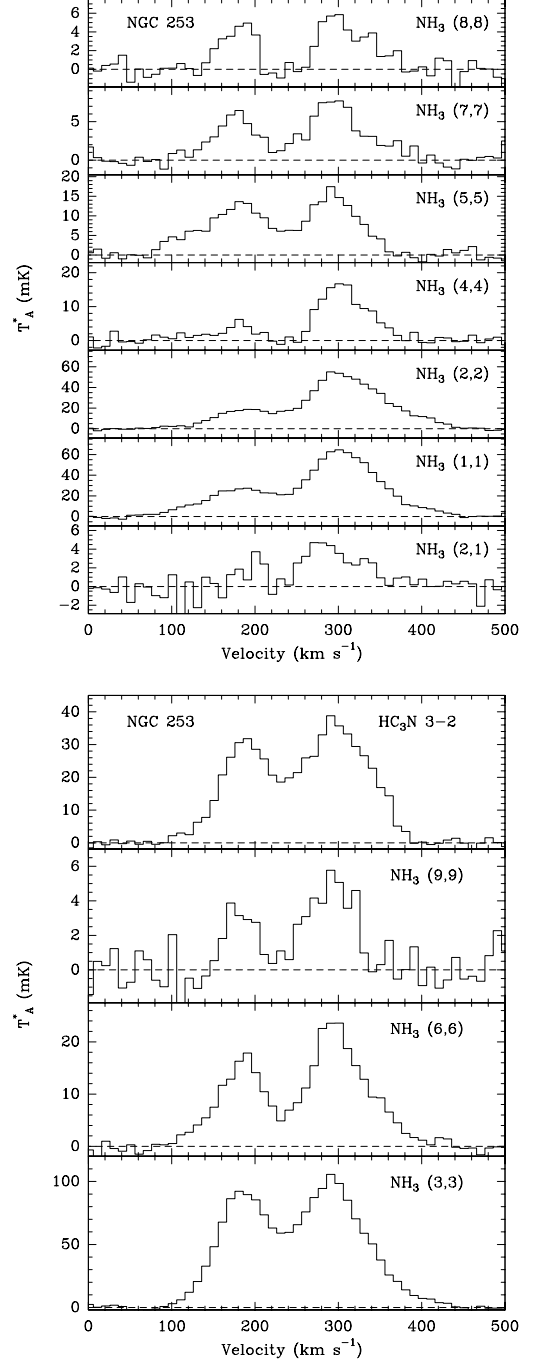


FIG. 2.— NH_3 and HC_3N $J=3-2$ spectra of NGC 253. The top panel shows spectra of para- NH_3 , while the bottom panel lists ortho- NH_3 and HC_3N $J=3-2$ spectra.

is the uncertainty associated with the collisional excitation rates used. Based on the analysis of the quantum mechanical calculations which went into the derivation of the para- NH_3 to para- H_2 collisional excitation rates presented by Danby et al. (1988), Danby et al. (1987) estimate that the calculated collisional excitation rates, which include all energy levels up to and including $J=5$ for para- NH_3 and $J=6$ for ortho- NH_3 , are accurate to 20% for kinetic temperatures $\lesssim 300$ K. We assume a similar level of accuracy for collisions involving ortho- NH_3

TABLE 3
EXTRAGALACTIC NH_3 MEASUREMENTS^a

Source	Transition	Fit ^b	T_A^* (mK)	v_{hel}^c (km s ⁻¹)	FW(HM/1I) ^d (km s ⁻¹)	$\int T_A^* dv^e$ (mK km s ⁻¹)	S_{cont} (mJy)
NGC 253	(1,1)	D,10	...	256.3	382.6	9347.2(92.9)	467
		G1,10	26.2(1.5)	176.1(2.2)	93.9(5.5)	2614.5(69.1)	
		G2,10	63.0(1.5)	306.6(0.9)	97.4(2.4)	6538.9(70.4)	
	(2,2)	D,10	...	263.5	368.2	7536.5(58.6)	
		G1,10	15.2(1.0)	176.1(0.0) ^f	93.9(0.0) ^f	1550.9(44.4)	
		G2,10	51.5(1.0)	309.9(1.4)	108.7(3.8)	5964.3(47.8)	
	(3,3)	D,10	...	260.3	373.3	15495.0(82.3)	
		G1,10	89.0(1.4)	182.7(1.0)	69.4(2.2)	6578.6(53.3)	
		G2,10	97.1(1.4)	291.6(1.1)	100.8(2.9)	10412.0(64.2)	
	(4,4)	D,10	...	237.4	328.5	1445.8(42.3)	
		G1,10	3.1(0.7)	176.1(0.0) ^f	93.9(0.0) ^f	310.9(34.0)	
		G2,10	16.5(0.7)	305.0(1.7)	63.3(3.8)	1112.9(27.9)	
	(5,5)	D,10	...	220.5	302.4	1485.1(52.8)	
		G1,10	12.1(1.0)	177.7(2.3)	102.2(6.5)	1316.4(46.1)	
		G2,10	15.5(1.0)	296.2(1.5)	66.6(3.5)	1099.9(37.2)	
	(6,6)	D,10	...	246.0	335.8	3081.1(63.0)	
		G1,10	16.4(1.1)	183.1(1.4)	63.5(3.7)	1110.5(41.1)	
		G2,10	22.2(1.1)	298.5(1.2)	81.2(3.3)	1920.7(46.5)	
	(7,7)	D,10	...	241.8	315.0	929.0(34.5)	
		G1,10	6.0(0.6)	176.5(2.1)	55.8(5.1)	355.3(21.8)	
		G2,10	7.4(0.60)	295.1(1.9)	75.7(5.6)	593.5(25.4)	
	(8,8)	D,10	...	172.8	84.2	613.6(22.9)	
		G1,10	5.0(0.8)	180.0(2.9)	42.2(5.6)	225.4(24.4)	
		G2,10	5.3(0.8)	305.5(3.6)	67.8(7.9)	384.9(30.9)	
	(9,9)	D,10	...	235.5	211.4	543.7(45.6)	
		G1,10	3.7(1.0)	181.9(2.6)	42.0(5.6)	165.3(30.5)	
		G2,10	5.3(1.0)	290.6(2.3)	65.4(5.4)	366.6(38.0)	
	(2,1)	D,10	...	229.2	324.9	432.3(33.2)	
		G2,10	4.2(0.8)	290.9(8.0)	86.0(26.4)	381.8(33.2)	
	(3,1)	...	(4.4)	
	(3,2)	...	(1.3)	
	(4,3)	...	(1.4)	
	(5,4)	...	(1.6)	
	HC ₃ N 3 – 2	D,10	...	241.1	299.6	5859.2(47.1)	
		G1,10	30.3(0.9)	187.2(1.2)	69.1(0.0)	2228.1(33.9)	
		G2,10	36.2(0.9)	298.8(1.2)	95.9(2.9)	3698.6(39.9)	
NGC 598	(1,1)	D,10	(1.1)	13
	(2,2)	D,10	(1.3)	
	(4,4)	D,10	(1.3)	
	(2,1)	D,10	(1.2)	
NGC 660	(1,1)	D,5	...	811.0	175.1	-1102.7(37.5)	78
		G1,5	-2.8(1.3)	769.3(9.7)	59.2(18.7)	-176.9(32.7)	
		G3,5	-16.6(1.3)	835.8(1.4)	49.1(3.0)	-865.2(29.8)	
		G4,5	-1.6(1.3)	974.6(9.6)	59.8(17.9)	-102.7(32.9)	
	(2,2)	D,5	...	800.9	212.2	-1384.6(46.6)	
		G1,5	-3.5(1.4)	765.0(0.0) ^f	64.7(15.1)	-243.7(38.6)	
		G2,5	-2.2(1.4)	800.0(0.0) ^f	26.5(18.7)	-62.5(24.7)	
		G3,5	-17.1(1.4)	837.9(2.0)	53.8(2.7)	-978.1(35.2)	
	(3,3)	G4,5	-1.4(1.4)	975.3(15.5)	82.3(34.7)	-122.6(43.5)	
		D,5	...	821.6	187.8	-1953.1(25.9)	
		G1,5	
		G2,5	-7.9(0.8)	785.0(1.8)	33.3(3.9)	-280.4(16.0)	
	(4,4)	G3,5	-20.3(0.8)	831.2(1.2)	54.6(2.0)	-1519.0(20.5)	
		G4,5	-3.2(0.8)	979.0(2.7)	37.4(7.1)	-126.7(17.0)	
		D,5	...	786.1	205.9	-863.9(32.3)	
		G1,5	-1.7(1.0)	765.0(0.0) ^f	88.1(43.7)	-157.1(31.7)	
	(5,5)	G2,5	-5.4(1.0)	795.0(0.0) ^f	36.7(9.7)	-210.7(20.4)	
		G3,5	-13.6(1.0)	838.8(1.3)	36.3(2.5)	-525.6(20.3)	
		D,5	...	825.3	178.3	-1042.4(28.2)	
		G1,5	
	(6,6)	G2,5	-4.0(1.0)	786.2(2.6)	30.1(4.9)	-129.3(17.7)	
		G3,5	-12.8(1.0)	829.1(1.7)	57.4(4.4)	-545.0(24.4)	
		G4,5	-1.4(1.0)	988.8(6.7)	40.5(28.7)	-41.9(20.5)	
		D,5	...	888.1	324.8	-1283.0(31.0)	
		G1,5	
		G2,5	-6.4(0.8)	792.0(0.0) ^f	30.0(0.0) ^f	-204.9(14.1)	
		G3,5	-13.1(0.8)	830.0(0.0) ^f	55.0(0.0) ^f	-769.5(19.1)	
		G4,5	-3.6(0.8)	985.9(3.7)	58.8(8.7)	-226.6(19.8)	

TABLE 3 — *Continued*

Source	Transition	Fit ^b	T_A^* (mK)	v_{hel}^c (km s ⁻¹)	FW(HM/ZI) ^d (km s ⁻¹)	$\int T_A^* dv^e$ (mK km s ⁻¹)	S_{cont} (mJy)
NGC 660	(7,7)	D,5	...	837.0	141.1	-277.2(18.1)	
		G1,5	
		G2,5	
		G3,5	-3.4(0.7)	825.6(3.1)	66.1(7.1)	-241.5(18.6)	
	(8,8)	G4,5	
		D,5	(2.2)	
		(9,9)	D,5	(3.5)	
		(2,1)	D,5	...	828.0	143.3	
		G1,5	-686.4(37.0)	
		G2,5	-2.8(1.4)	789.5(4.6)	27.4(17.2)	-82.5(24.3)	
		G3,5	-12.7(1.4)	838.1(1.4)	42.7(3.7)	-577.9(30.3)	
		G4,5	-1.3(1.4)	970.0(0.0) ^f	40.0(0.0) ^f	-55.9(29.4)	
	(3,1)	D,5	...	839.5	132.0	-782.7(27.2)	
		G1,5	
		G2,5	-2.9(1.0)	789.0(0.0) ^f	35.0(0.0) ^f	-108.0(36.0)	
		G3,5	-10.6(1.0)	827.7(1.6)	46.7(4.5)	-527.5(42.0)	
	(3,2)	G4,5	
		D,5	...	845.8	325.0	-563.9(26.4)	
		G1,5	
		G2,5	-3.9(1.0)	789.0(0.0) ^f	35.0(0.0) ^f	-143.6(24.0)	
		G3,5	-7.3(1.0)	829.1(1.7)	44.4(4.0)	-346.7(27.0)	
		G4,5	-2.5(1.0)	980.8(3.7)	39.1(6.5)	-105.0(18.0)	
		(4,3)	D,5	...	854.7	325.0	
		G1,5	-646.0(29.1)	
		G2,5	-3.9(1.1)	789.0(0.0) ^f	35.0(0.0) ^f	-146.2(29.0)	
		G3,5	-9.0(1.1)	831.9(1.7)	34.5(4.1)	-329.3(33.0)	
		G4,5	-3.9(1.1)	988.0(3.7)	32.2(7.9)	-133.0(29.0)	
		(5,4)	D,5	...	830.0	95.0	
		G1,5	-148.3(21.6)	
		G2,5	
		G3,5	-2.4(1.0)	830.0(0.0) ^f	40.0(0.0) ^f	-102.4(27.0)	
		G4,5	
IR 01418+1651	HC ₃ N 3 – 2	D,5	(2.7)	13
		(1,1)	D,10	(1.6)	
		(2,2)	D,10	(1.6)	
		(4,4)	D,10	(1.5)	
		(2,1)	D,10	(1.6)	
NGC 891	(1,1)	D,5	...	540.5	94.4	124.3(24.3)	44
		G1,5	2.5(1.1)	543.9(3.4)	45.3(7.7)	120.2(25.0)	
		(2,2)	D,5	(1.1)	
		(4,4)	D,5	(1.0)	
Maffei 2	(1,1)	D,5	(1.1)	35
		D,10	...	-32.0	328.8	3068.5(36.8)	
		G1,10	21.5(0.6)	-68.5(1.7)	82.0(4.5)	1878.0(27.6)	
		G2,10	15.8(0.6)	27.4(2.2)	70.6(5.0)	1269.0(25.6)	
	(2,2)	D,10	...	-28.3	251.8	1779.8(45.0)	
		G1,10	12.9(0.9)	-68.1(2.0)	69.5(4.8)	955.9(35.5)	
		G2,10	9.3(0.9)	21.2(3.1)	78.0(6.6)	771.4(37.6)	
		(4,4)	D,10	...	247.4	398.6(29.4)	
		G1,10	4.4(0.6)	-70.6(2.2)	47.2(6.5)	221.9(19.3)	
		G2,10	2.2(0.6)	34.6(5.9)	73.9(14.1)	398.6	
		(2,1)	D,10	(0.7)	
		(1,1)	D,10	(1.7)	
NGC 1144	(2,2)	D,10	(1.6)	42
		(4,4)	D,10	(1.7)	
		(2,1)	D,10	(2.7)	
		(1,1)	D,10	
NGC 1365	(1,1)	D,10	...	1646.0	363.2	1972.7(80.0)	40
		G1,10	8.5(1.3)	1573.6(2.7)	112.0(7.0)	1014.0(66.6)	
		G2,10	8.8(1.3)	1739.3(2.6)	110.5(6.8)	1040.9(66.2)	
		(2,2)	D,10	...	302.2	1255.7(68.9)	
		G1,10	7.4(1.3)	1572.7(3.6)	116.1(9.8)	918.4(64.0)	
		G2,10	4.4(1.3)	1721.8(5.5)	85.0(10.5)	397.2(55.0)	
		(4,4)	D,10	...	122.1	157.3(66.6)	
		G1,10	1.7(1.5)	1758.6(10.6)	85.0(0.0) ^f	157.3(66.6)	
		(2,1)	D,10	(1.6)	
		(1,1)	D,5	...	186.4	2191.8(37.3)	
IC 342	(1,1)	G1,5	33.3(1.2)	25.3(2.8)	51.1(3.3)	1810.6(29.2)	75
		G2,5	9.1(1.2)	55.3(4.0)	36.7(5.2)	354.2(24.8)	
		(2,2)	D,5	...	150.7	1135.9(28.6)	
		G1,5	17.7(1.0)	19.1(1.7)	36.7(2.5)	691.7(21.2)	
		G2,5	13.0(1.0)	48.6(1.9)	31.4(2.7)	434.8(19.6)	

TABLE 3 — *Continued*

Source	Transition	Fit ^b	T_A^* (mK)	v_{hel}^c (km s ⁻¹)	FW(HM/ZI) ^d (km s ⁻¹)	$\int T_A^* dv^e$ (mK km s ⁻¹)	S_{cont} (mJy)
IC 342	(4,4)	D,5	...	28.6	98.4	371.7(21.2)	
		G1,5	6.1(1.0)	25.8(2.2)	41.3(4.5)	267.5(21.0)	
		G2,5	2.8(1.0)	52.1(3.8)	31.0(0.0) ^f	92.4(19.0)	
	(2,1)	D,5	...	43.9	76.4	81.1(19.1)	
		G2,5	2.4(1.0)	48.7(2.9)	31.7(5.7)	81.1(19.1)	
	(3,3)	D,5	...	32.4	149.6	2106.4(35.5)	
		G1,5	26.1(1.3)	20.9(1.1)	41.9(3.7)	1165.7(28.0)	
		G2,5	24.7(1.3)	48.7(1.0)	33.5(3.0)	880.0(25.0)	
	(5,5)	D,5	...	39.0	81.6	244.2(22.1)	
		G1,5	5.8(1.1)	25.3(0.0) ^f	28.7(3.9)	175.7(19.7)	
		G2,5	3.7(1.1)	55.3(0.0) ^f	23.1(4.2)	92.0(17.7)	
	(6,6)	D,5	...	45.0	125.22	375.5(30.3)	
		G1,5	3.4(1.2)	20.9(0.0) ^f	49.2(8.6)	176.3(28.6)	
		G2,5	3.7(1.2)	48.7(0.0) ^f	52.6(8.9)	207.5(29.5)	
	(7,7)	D,5	(1.5)	
NGC 2146	(1,1)	D,10	(0.8)	130
	(2,2)	D,10	(0.8)	
	(4,4)	D,10	(0.9)	
M 82	(2,1)	D,10	(0.8)	731
	(1,1)	D,10	(3.7)	
	(2,2)	D,10	(3.0)	
	(4,4)	D,10	(2.8)	
M 82SW	(2,1)	D,10	(2.5)	776
	(1,1)	D,10	...	118.1	150.7	840.1(52.1)	
		G1,10	8.0(1.1)	119.9(2.8)	104.5(6.5)	888.2(52.1)	
	(2,2)	D,10	...	130.7	177.9	561.4(71.5)	
NGC 3079		G1,10	4.7(1.7)	132.2(6.3)	122.1(15.3)	607.5(88.9)	174
	(4,4)	D,10	(1.0)	
	(2,1)	D,10	(1.3)	
	(1,1)	D,5	...	1087.8	229.2	-1941.5(40.2)	
		G1,5	-6.4(1.2)	1024.4(2.7)	56.0(6.9)	-381.0(29.8)	
		G2,5	-34.8(1.2)	1115.9(0.4)	40.8(1.1)	-1512.3(25.5)	
	(2,2)	D,5	...	1077.7	260.0	-2326.1(39.0)	
		G1,5	-8.0(1.1)	1017.4(2.7)	65.9(7.2)	-563.5(29.5)	
		G2,5	-42.4(1.1)	1114.7(0.4)	37.0(1.0)	-1673.0(22.1)	
	(4,4)	D,5	...	1069.7	218.6	-1831.2(43.4)	
		G1,5	-6.5(1.3)	1019.9(3.6)	64.5(10.0)	-447.3(35.3)	
		G2,5	-36.6(1.3)	1115.3(0.5)	35.1(1.2)	-1366.6(26.1)	
	(2,1)	D,5	(1.5)	
	(3,3)	D,5	(1.2)	
	(5,5)	D,5	...	1073.2	193.6	-1031.1(39.4)	
		G1,5	-4.6(1.3)	1016.9(3.1)	44.5(7.5)	-216.2(28.4)	
		G2,5	-22.5(1.3)	1115.2(0.5)	33.9(1.5)	-812.1(24.7)	
	(6,6)	D,5	...	1058.4	192.5	-830.9(54.6)	
		G1,5	-2.5(1.8)	1000.5(8.9)	59.7(17.9)	-161.5(45.7)	
		G2,5	-25.7(1.8)	1116.4(0.5)	28.3(1.2)	-775.2(31.5)	
	(7,7)	D,5	...	1069.9	228.6	-884.8(33.2)	
		G1,5	-4.1(1.0)	1021.1(6.9)	79.5(17.7)	-347.1(29.4)	
		G2,5	-13.6(1.0)	1116.5(1.4)	36.6(4.0)	-529.7(20.0)	
	(8,8)	D,5	(0.8)	
	(9,9)	D,5	...	1074.3	187.0	-532.8(43.5)	
		G1,5	-3.6(1.4)	1028.4(5.7)	40.6(16.9)	-155.4(30.4)	
		G2,5	-10.4(1.4)	1117.3(1.7)	31.0(5.2)	-342.4(26.5)	
NGC 3628	HC ₃ N 3 - 2	D,5	(1.4)	138
		D,5	(1.4)	
		D,5	(1.2)	
		D,5	(1.1)	
		D,5	(1.1)	
	(1,1)	D,10	(0.9)	
	(2,2)	D,10	(1.1)	
	(4,4)	D,10	(1.1)	
	(2,1)	D,10	(1.3)	
NGC 3690	(1,1)	D,10	(2.1)	147
	(2,2)	D,10	(1.6)	
	(4,4)	D,10	(1.6)	
	(2,1)	D,10	(1.8)	
NGC 4214	(1,1)	D,10	(1.7)	147
	(2,2)	D,10	(1.3)	
	(4,4)	D,10	(1.4)	
	(2,1)	D,10	(1.5)	

TABLE 3 — *Continued*

Source	Transition	Fit ^b	T_A^* (mK)	v_{hel}^c (km s ⁻¹)	FW(HM/ZI) ^d (km s ⁻¹)	$\int T_A^* dv^e$ (mK km s ⁻¹)	S_{cont} (mJy)
NGC 4418	(1,1)	D,10	(0.6)	147
	(2,2)	D,10	(0.6)	
	(4,4)	D,10	(0.5)	
Mrk 231	(2,1)	D,10	(0.4)	173
	(1,1)	D,10	(2.6)	
	(2,2)	D,10	(2.3)	
	(4,4)	D,10	(2.6)	
IC 860	(2,1)	D,10	(2.6)	27
	(1,1)	D,10	...	3894.2	237.9	-305.4(24.1)	
		G1,10	-3.3(0.5)	3901.6(5.9)	86.3(14.6)	-301.9(21.8)	
	(2,2)	D,10	...	3837.8	316.9	-829.8(22.6)	
		G1,10	-5.8(0.4)	3874.0(3.8)	129.7(9.6)	-797.4(21.7)	
	(4,4)	D,10	...	3846.3	262.2	-430.8(25.7)	
		G1,10	-3.0(0.5)	3881.0(6.1)	136.4(15.7)	-430.8(25.7)	
	(2,1)	D,10	...	3935.2	339.0	-390.5(38.8)	
		G1,10	-2.2(0.7)	3908.1(7.8)	168.0(20.2)	-397.0(40.9)	
	(3,3)	D,10	...	3851.5	247.4	-938.6(63.8)	
		G1,10	-8.8(1.3)	3881.7(2.5)	103.4(5.8)	-965.2(32.2)	
		G2,10	-2.4(1.3)	3761.6(4.8)	27.9(10.8)	-71.0(61.9)	
	(5,5)	D,10	...	3829.5	236.2	-529.2(140.3)	
		G1,10	-5.3(2.9)	3864.8(6.6)	119.4(16.8)	-671.0(149.6)	
		G2,10	-2.6(2.9)	729.3(6.2)	28.0(0.0) ^f	-78.7(72.3)	
	(6,6)	D,10	...	3913.3	193.2	-538.4(46.4)	
		G1,10	-6.4(1.1)	3904.9(3.0)	75.9(7.4)	-513.5(43.7)	
M 83	(7,7)	D,10	...	3908.4	181.2	-194.4(54.5)	76
		G1,10	-3.3(1.3)	3894.9(6.9)	65.8(15.1)	-220.2(49.3)	
	(1,1)	D,10	...	505.6	194.8	897.4(46.4)	
		G1,10	10.6(1.1)	500.1(1.7)	79.3(4.2)	897.4(46.4)	
	(2,2)	D,10	...	533.5	181.1	606.6(37.1)	
		G1,10	6.3(0.8)	507.6(3.5)	90.5(9.2)	606.6(37.1)	
	(4,4)	D,10	(1.1)	
IR 15107+0724	(2,1)	D,10	(0.8)	15.4
	(1,1)	D,10	...	3974.6	386.8	-502.4(55.9)	
		G1,10	-2.1(1.0)	3946.2(17.5)	223.0(0.0) ^f	-490.0(74.0)	
	(2,2)	D,10	...	3900.0	400.0	-1638.6(67.7)	
		G1,10	-6.8(1.0)	3905.6(5.4)	223.1(12.9)	-1597.5(80.0)	
Arp 220	(4,4)	D,10	...	3989.8	281.1	-240.9(55.1)	140.0
		G1,10	-1.5(1.0)	3976.5(25.9)	223.0(0.0) ^f	-351.4(83.0)	
	(1,1)	D,10	...	5310.0	~ 300.0	-860.5(72.9)	
		G1,10	-0.2(0.7)	5290.0(0.0)	150.0(0.0)	-34.7(38.8)	
		G2,10	-6.5(0.7)	5460.0(0.0)	147.7(13.8)	-730.3(38.5)	
	(2,2)	D,10	...	5231.0	869.0	-6338.3(72.9)	
		G1,10	-10.8(0.7)	5290.0(0.0)	176.1(10.0)	-2020.8(42.0)	
		G2,10	-13.0(0.7)	5460.0(0.0)	189.0(8.1)	-2607.6(43.5)	
		G3,10	-2.4(0.7)	5200.0(0.0)	534.3(73.1)	-1370.6(73.3)	
	(4,4)	D,10	...	5363.6	715.9	-1502.6(65.6)	
		G1,10	-3.4(0.8)	5290.0(0.0)	241.8(17.3)	-879.9(57.0)	
		G2,10	-4.8(0.8)	5460.0(0.0)	308.2(17.3)	-669.0(64.4)	
	(10,9)	G2,10	-2.7(0.8)	5449.8(8.4)	198.0(19.3)	-568.4(51.6)	
	(3,3)	D,10	...	5310.0	710.0	-4827.3(212.2)	
		G1,10	-9.7(2.3)	5292.7(44.0)	325.0(46.2)	-3352.5(193.7)	
		G2,10	-6.6(2.3)	5437.6(31.7)	205.4(58.5)	-1432.5(154.0)	
	OH23827	G2,10	-7.2(2.3)	5464.1(13.2)	288.4(31.4)	-2213.1(213.1)	
	(5,5)	D,10	...	5350.4	610.5	-2211.7(107.4)	
		G1,10	-6.2(1.4)	5290.0(0.0)	221.6(18.0)	-1453.9(97.1)	
		G2,10	-4.2(1.4)	5460.0(0.0)	179.4(22.2)	-795.2(87.4)	
(6,6)	D,10	5394.4	882.8	-2079.1(70.5)	
		G1,10	-1.9(0.8)	5290.0(0.0)	357.4(66.5)	-728.6(67.3)	
		G2,10	-4.0(0.8)	5460.0(0.0)	331.2(24.6)	-1401.1(64.8)	
	(7,7)	D,10	...	5396.6	685.2	-1978.1(79.5)	
		G1,10	-2.1(1.0)	5290.0(0.0)	246.2(35.7)	-541.1(71.5)	
		G2,10	-5.0(1.0)	5460.0(0.0)	248.0(14.4)	-1330.4(71.8)	
	(8,8)	D,10	...	5396.6	430.4	-1429.4(38.8)	
		G1,10	-2.0(0.6)	5290.0(0.0)	286.1(33.9)	-622.8(47.7)	
		G2,10	-3.4(0.6)	5460.0(0.0)	237.5(17.7)	-857.8(43.4)	
	(9,9)	D,10	(1.0)	

TABLE 3 — *Continued*

Source	Transition	Fit ^b	T_A^* (mK)	v_{hel}^c (km s ⁻¹)	FW(HM/ZI) ^d (km s ⁻¹)	$\int T_A^* dv^e$ (mK km s ⁻¹)	S_{cont} (mJy)
NGC 6946	(1,1)	D,10	...	49.2	265.9	859.6(20.5)	33
		G1,10	3.1(0.4)	-8.0(0.0) ^f	68.1(5.1)	227.1(15.6)	
		G2,10	5.5(0.4)	64.5(3.4)	110.8(7.4)	646.9(19.8)	
	(2,2)	D,10	...	42.7	231.1	529.9(18.1)	
		G1,10	1.1(0.4)	-8.0(0.0) ^f	58.7(26.8)	69.3(13.7)	
		G2,10	3.1(0.4)	54.5(11.8)	123.5(16.7)	411.4(19.9)	
	(4,4)	D,10	(0.5)	
	(2,1)	D,10	(0.4)	
NGC 6951	(1,1)	D,10	(1.1)	12
	(2,2)	D,10	(1.5)	
	(4,4)	D,10	(1.3)	
	(2,1)	D,10	(1.1)	
	(2,1)	D,10	(1.1)	

^a Table entries in parentheses are standard deviations or, in case of non-detections, RMS noise levels.

^b Gn,m / D,m \equiv Gaussian component number n / Direct measurement results with spectral resolution m km s⁻¹.

^c Heliocentric optical velocity frame.

^d Full-width half maximum (FWHM) given for gaussian fits; full-width zero intensity (FWZI) given for direct measurements.

^e Derived from direct integration of the FWZI line profile.

^f NGC 253: NH₃ (2,2) and (4,4) G1 fixed v_{hel} and FWHM to NH₃ (1,1) values; NGC 660: NH₃ (2,2) and (4,4) G1 and G2 fixed v_{hel} to nominal velocity for this component (see Section 5.3), NH₃ (6,6) G2 and G3, and NH₃ (2,1) G4 fixed v_{hel} and FWHM to nominal and/or best-fit values for this component (see Section 5.3), NH₃ (3,1), (3,2), and (4,3) G2 and (5,4) G3 fixed v_{hel} and FWHM to NH₃ (2,1) values; NGC 1365: NH₃ (4,4) fixed v_{hel} to NH₃ (2,2) value; IC 342: NH₃ (4,4) G2 fixed FWHM to NH₃ (2,2) value, NH₃ (5,5) fixed v_{hel} to NH₃ (1,1) value, and NH₃ (6,6) fixed v_{hel} to NH₃ (3,3) value; IC 860: NH₃ (5,5) G2 fixed FWHM to NH₃ (3,3) value; IR 15107+0724: NH₃ (1,1) G1 fixed FWHM to NH₃ (2,2) value, NH₃ (4,4) G1 fixed FWHM to NH₃ (1,1) value; NGC 6946: NH₃ (1,1) and (2,2) G1 fixed v_{hel} to -8.0 km s⁻¹ from H₂CO 2₁₁ - 2₁₂ value (Mangum et al. 2013).

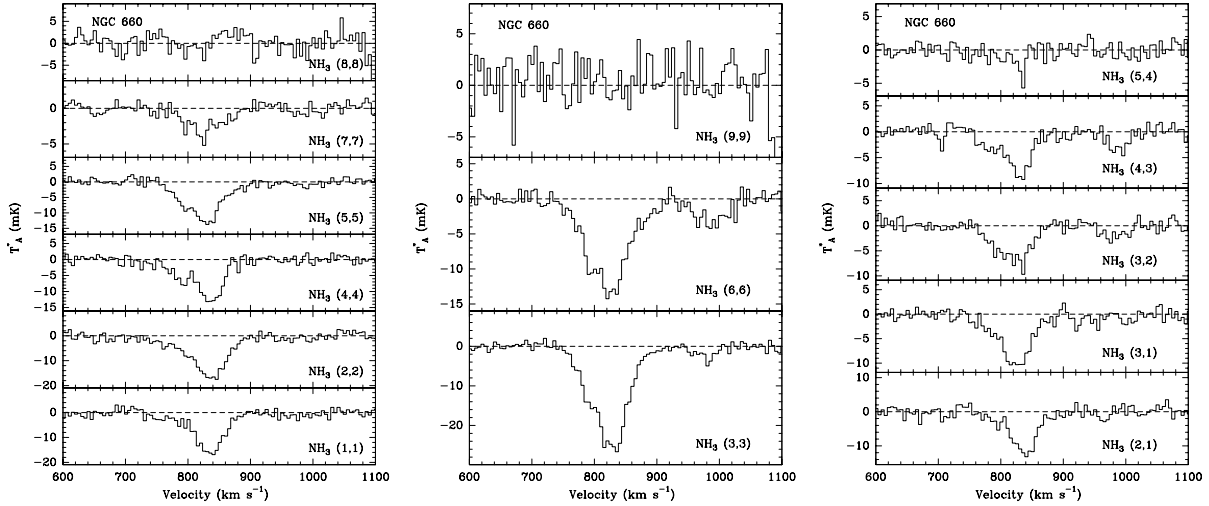


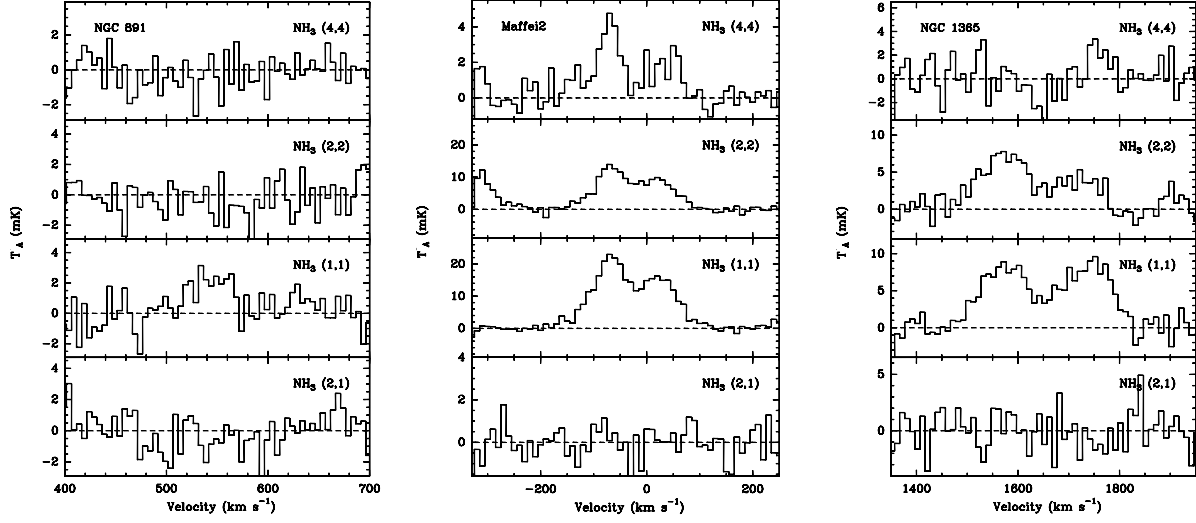
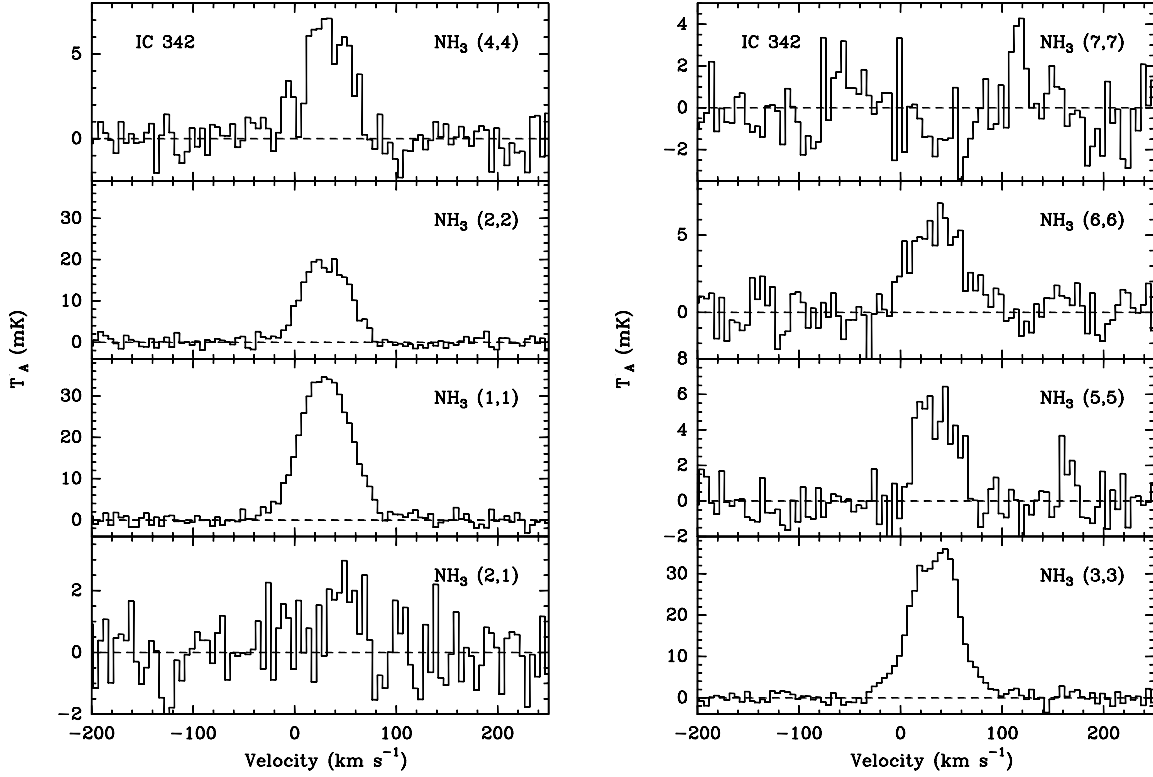
FIG. 3.— NH₃ spectra of NGC 660. The left, middle, and right panels show spectra of metastable ($J=K$) para-NH₃, metastable ortho-NH₃, and non-metastable ($J \neq K$) NH₃, respectively.

when $J < 6$. Therefore, all physical conditions predicted by our LVG model which use the Danby et al. rates are limited to an accuracy of no better than 20% when constrained by measurements of NH₃.

As one can see from the listing of observed NH₃ frequencies and their associated energies (Table 1), we measure several NH₃ transitions which include energy levels not included in the Danby et al. (1988) excitation rate calculations. In order to model the excitation of all measured NH₃ transitions we have extended the Danby et al. (1988) excitation rates using the prescription set forth in Flower et al. (1995). This extrapolation to higher energy levels assumes that the collisional de-excitation rates for NH₃ can be assumed to be the same as those computed

by Danby et al. (1988) for 300 K and for the same change in rotational quantum number J . An average of the existing excitation rates for a given $(\Delta J, \Delta K)$ were used to extrapolate to higher (J, K) . As noted by Flower et al. (1995), this extrapolation procedure is rather arbitrary, and we treat the results obtained from these extrapolated excitation rates with due caution.

After investigation of the limitations imposed by the iterative solution speed as a function of the number of levels in our LVG model, a uniform limit of $E \leq 1600$ K and quantum number $K \leq 10$ was chosen as the boundary for the extended para- and ortho-NH₃ excitation rates. This resulted in a total of 84 and 43 levels for para- and ortho-NH₃, respectively. The energy levels and measured

FIG. 4.— NH_3 spectra of NGC 891 (left), Maffei 2 (middle), and NGC 1365 (right).FIG. 5.— NH_3 spectra of IC 342.

transitions included in our LVG model analysis are shown in Figure 11.

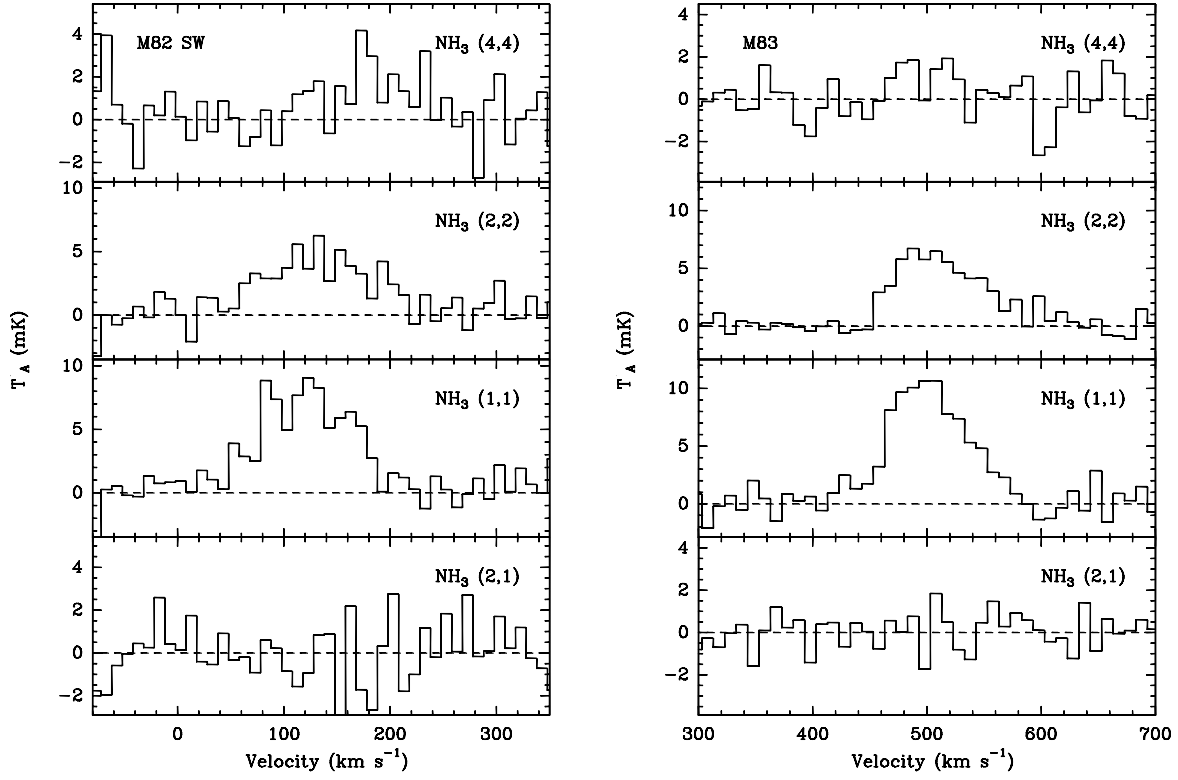
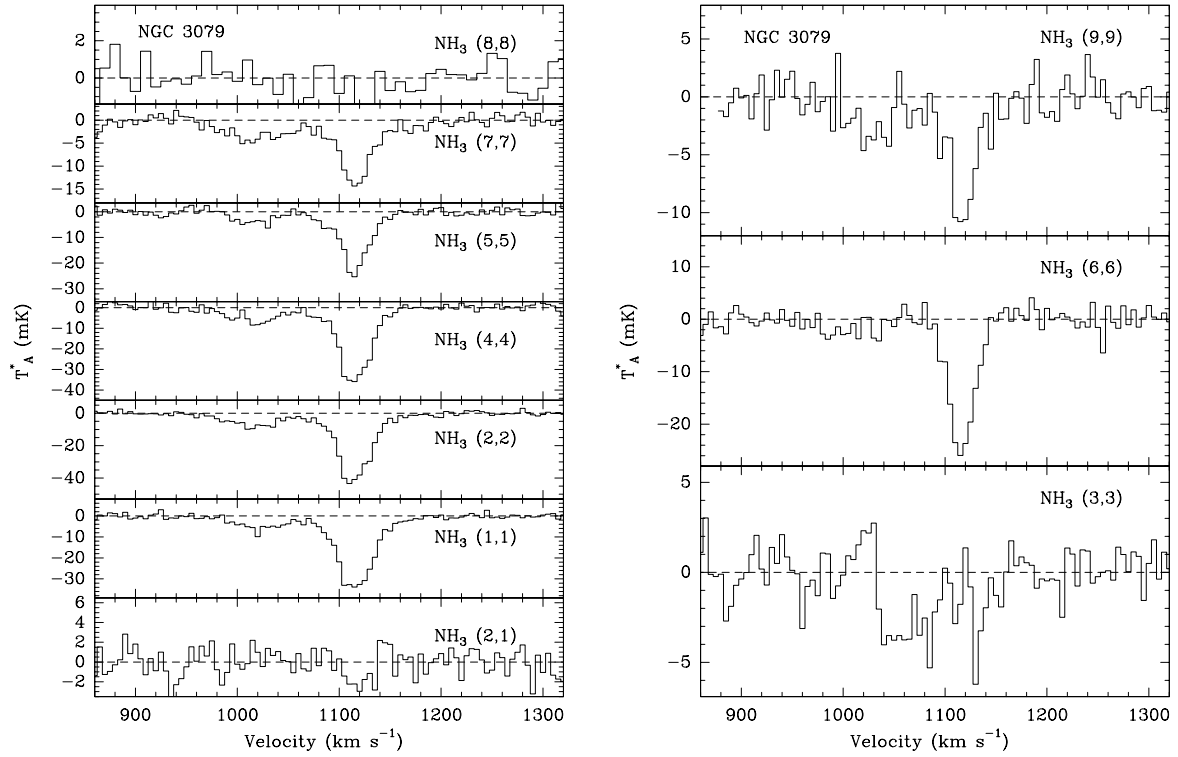
Model grids of predicted NH_3 transition intensities over ranges in spatial density, para- or ortho- NH_3 column density per velocity gradient, and kinetic temperature were made to accommodate the requirements for fitting to several types of sources. Both para- and ortho- NH_3 model fits were required, in addition to model grids which incorporated background continuum and infrared emission sources. Table 4 lists the LVG model grids and their ranges in spatial density and NH_3 column density,

temperature ranges, increments, and assumed continuum temperature. Measured NH_3 transition ratios were fit to these LVG model grids using two methods:

1. χ^2 goodness-of-fit estimation of line ratios using:

$$\chi^2 = \sum_{i=1}^{i=n-1} \frac{\left| \frac{\int T_A^* dv(i)}{\int T_A^* dv(i+1)} - \frac{\int T_{\text{model}} dv(i)}{\int T_{\text{model}} dv(i+1)} \right|^2}{\left[\sigma \left(\frac{\int T_A^* dv(i)}{\int T_A^* dv(i+1)} \right) \right]^2} \quad (3)$$

where n is the number of transitions measured in

FIG. 6.— NH_3 spectra of M82SW (left) and M83 (right).FIG. 7.— Para- NH_3 (left panel) and ortho- NH_3 (right panel) spectra of NGC 3079.

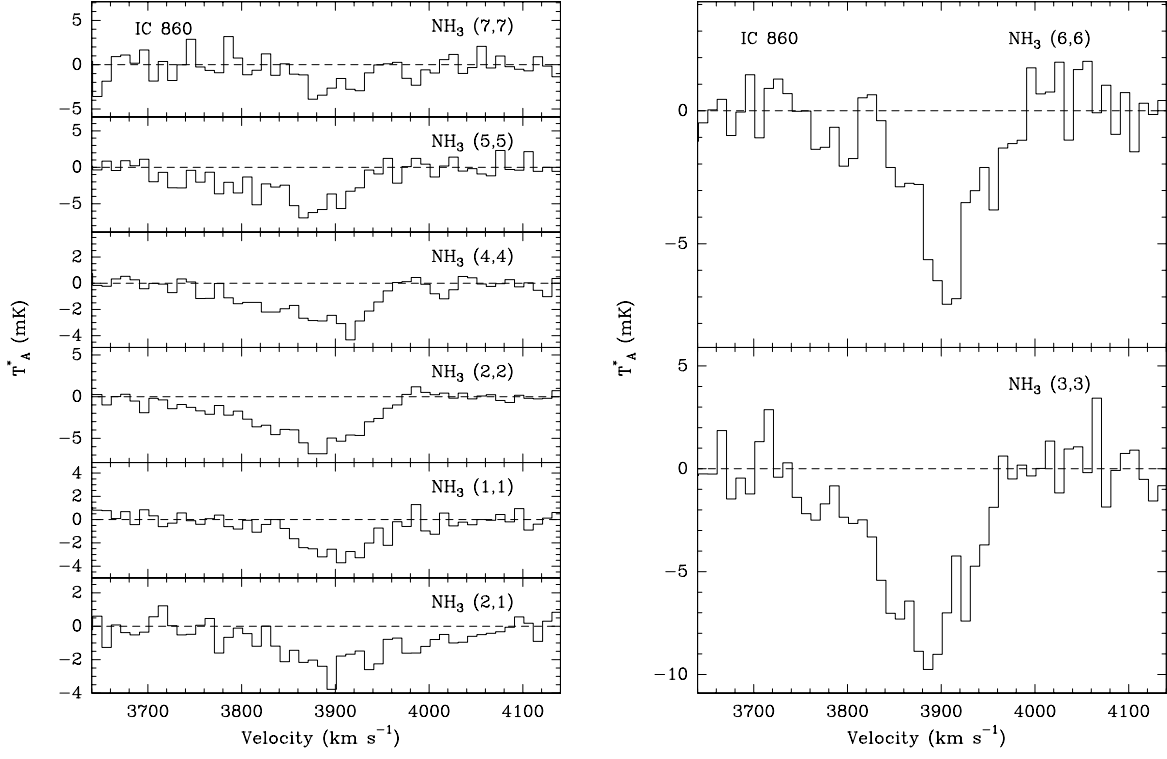


FIG. 8.— Para-NH₃ (left panel) and ortho-NH₃ (right panel) spectra of IC 860.

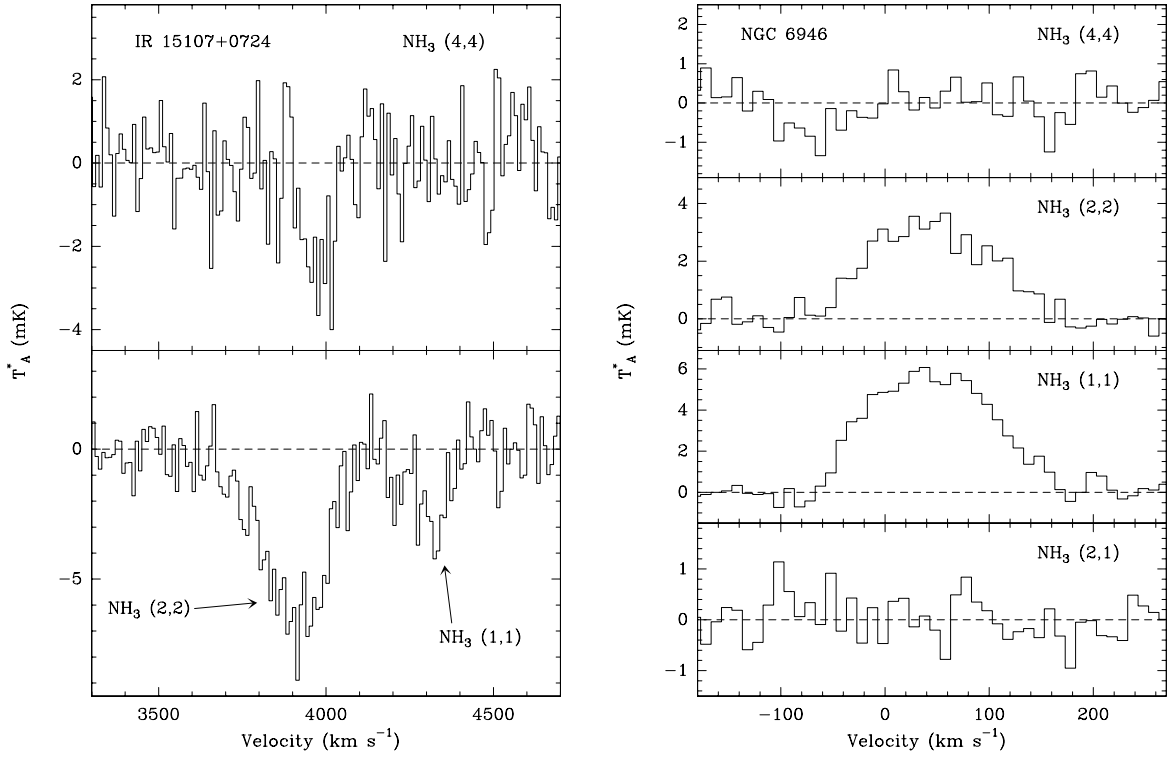


FIG. 9.— NH₃ spectra of IR 15107+0724 (left) and NGC 6946 (right). For the IR 15107+0724 NH₃ (1,1) and (2,2) spectrum the velocity scale is referenced to the NH₃ (2,2) transition frequency.

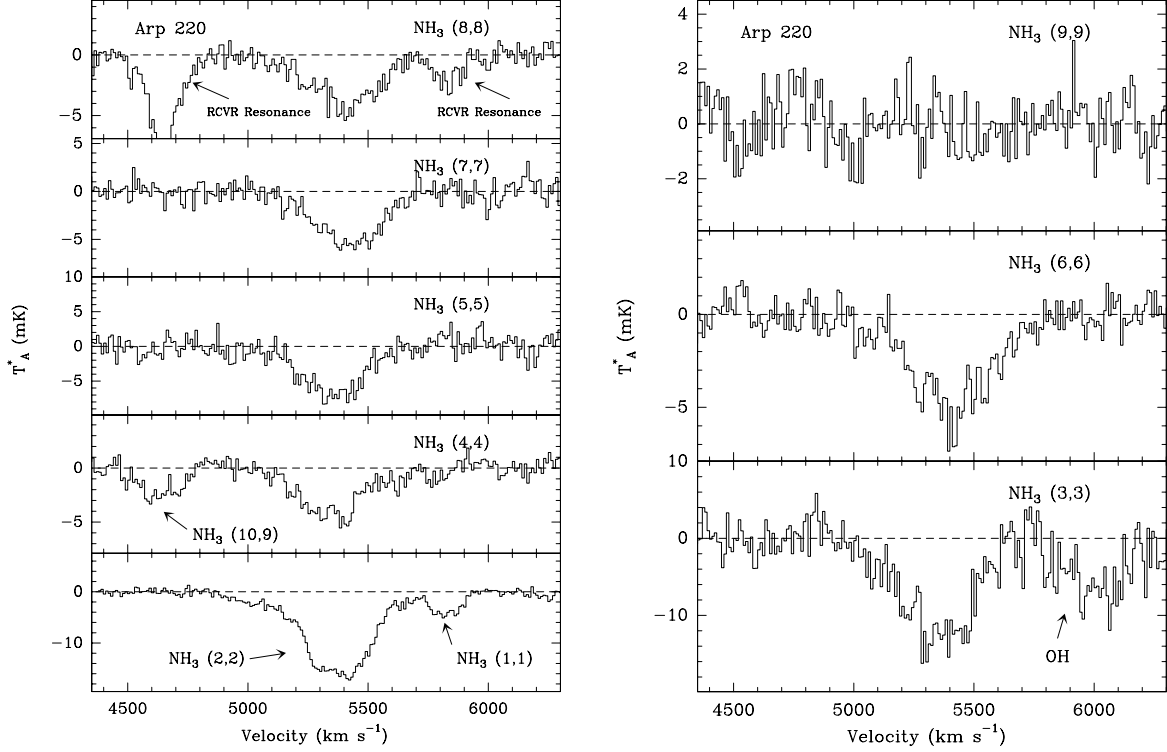


FIG. 10.— Para-NH₃ (left panel) and ortho-NH₃ (right panel) spectra of Arp 220. For the NH₃ (1,1) and (2,2) spectrum the velocity scale is referenced to the NH₃ (2,2) transition frequency.

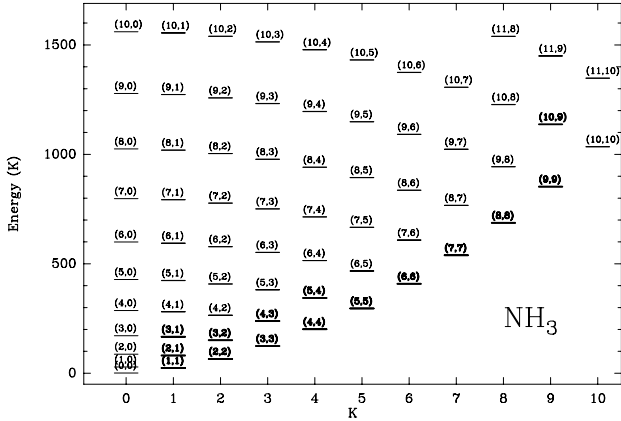


FIG. 11.— NH₃ energy levels included in our LVG model analysis. Levels involving measured transitions are shown in **bold**.

a single galaxy.

2. NH₃ transition ratio best-fit using measured value $\pm\sigma$ comparisons to modelled ratios. When more than two transition ratios are considered, the most extreme ranges in measurement uncertainty have been used to calculate the best-fit T_K .

The values of χ^2 which correspond to 1σ , 2σ , and 3σ confidence in goodness of fit are dependent upon the

number of degrees-of-freedom (DOF) associated with a given model fit. The number of DOF is given by the difference between the number of NH₃ transitions measured and the number of free parameters considered in the LVG model fit. The NH₃ transition ratios included in this analysis show only weak dependence on spatial density and column density within the modeled ranges of these physical conditions. Specifically, over our modelled range of spatial density and NH₃ column density the (1,1)/(2,2), (2,2)/(4,4), and (5,5)/(7,7) ratios vary by $\lesssim 15\%$, with variations of $\lesssim 5\%$ over $\sim 90\%$ of this modelled range. Figure 12 shows examples of the LVG-modelled NH₃ (1,1)/(2,2) and (2,2)/(4,4) transition ratios as functions of $n(\text{H}_2)$ and para-NH₃ column density per unit line width. With a weak dependence on spatial density and NH₃ column density, we assume $\text{DOF} = \text{number of measured NH}_3 \text{ transitions considered minus one}$. For $\text{DOF} = 1, 2, 3$, and 4 the χ^2 values for 1σ , 2σ , and 3σ confidence intervals are (1.0, 4.0, 9.0), (2.3, 6.2, 11.8), (3.5, 8.0, 14.2), and (4.7, 9.7, 16.3), respectively.

Table 5 lists the derived LVG model best-fit kinetic temperatures for the 13 galaxies where we detect at least one NH₃ transition and have a limit to at least one other NH₃ transition (Table 3). Discussions of these LVG model kinetic temperature fits, along with a comparison to previous NH₃ measurements of individual galaxies, are given in §5.3.

TABLE 4
LVG MODEL GRID PARAMETERS

NH ₃ Species	$n(\text{H}_2), \Delta \log(n(\text{H}_2))$ (cm ⁻³)	$N', \Delta \log(N')^a$ (cm ⁻² /km s ⁻¹)	$T_K, \Delta T_K$ (K)	T_c (K)	Used For
para	$10^4 - 10^7, (0.03, 0.06)$	$10^{11} - 10^{14}, (0.04, 0.08)$	15–300, 3	T_{cmb}	Emission
para	$10^4 - 10^7, (0.03, 0.06)$	$10^{11} - 10^{14}, (0.04, 0.08)$	10–300, 5	$T_{cmb}+300$	Absorption
para	$10^4 - 10^7, (0.03, 0.06)$	$10^{11} - 10^{14}, (0.04, 0.08)$	15–300, 3	$T_{cmb}+T_c^b$	Absorption
ortho	$10^4 - 10^7, (0.03, 0.06)$	$10^{11} - 10^{14}, (0.04, 0.08)$	15–300, 3	T_{cmb}	Emission
para	$10^4 - 10^9, (0.05, 0.10)$	$10^{12} - 10^{17}, (0.05, 0.10)$	15–300, 3	$T_{cmb}+300$	NGC 660
ortho	$10^4 - 10^9, (0.05, 0.10)$	$10^{12} - 10^{17}, (0.05, 0.10)$	15–300, 3	$T_{cmb}+300$	NGC 660
para	$10^4 - 10^7, (0.03, 0.06)$	$10^{11} - 10^{14}, (0.04, 0.08)$	15–300, 3	$T_{cmb}+T_{IR}^c$	NGC 253, IC 342

^a $N' \equiv$ Column density per velocity gradient increment $N(\text{species-NH}_3)/\Delta v$.

^b Separate model cubes with $T_c = 50, 100, 200, 300, 400$, and 500 K.

^c $T_{IR} = T_{dust} = 34$ K for NGC 253 and IC 342.

TABLE 5
STAR FORMING GALAXY DERIVED KINETIC TEMPERATURES

Source ^a	T_{dust}^b (K)	T_K (K)	Notes ^c	Fit Type ^d
NGC 253	34	$78 \pm 22 / > 150$	PF,MTC,MVC	R(5,2)
NGC 253 NE	...	$38 \pm 9 / 73 \pm 9 / > 150$	PF,MTC	R(5,2)
NGC 253 SW	...	$78 \pm 22 / > 150$	PF,MTC	R(5,2)
NGC 660	37	160 ± 96^e
NGC 660 G1	...	149 ± 72^f	GF	$\chi^2(2)$
NGC 660 G2	...	$\geq 150^f$	PF	R(2,1)
NGC 660 G3	...	$\geq 100^f$	PF	R(4,1)
NGC 660 G4	...	163 ± 93^f	GF	$\chi^2(4,1)$
NGC 891	28	< 30		
Maffei 2	40 ^g	$43 \pm 6 / 79 \pm 6$	PF,MTC	R(2)
Maffei 2 G1	...	$40 \pm 3 / 82 \pm 6$	PF,MTC	R(2)
Maffei 2 G2	...	$50 \pm 10 / 79 \pm 9$	PF,MTC	R(2)
NGC 1365	32	50 ± 11	GF	R(2)
NGC 1365 G1	...	110^{+50}_{-40}	GF	R(2)
NGC 1365 G2	...	29 ± 6	GF	R(2)
IC 342	30	~ 150	PF,MTC	$\chi^2(4,1)$
IC 342 G1	...	$24 \pm 7 / 115 \pm 17 / > 140$	GF,MTC	R(3,1)
IC 342 G2	...	$75 \pm 14 / > 185$	GF,MTC	R(4,1)
M 82 SW	45	58 ± 19	GF	R(2)
NGC 3079	32	> 150	PF	$\chi^2(4,1)$
NGC 3079 G1	...	> 100	PF	$\chi^2(4,1)$
NGC 3079 G2	...	> 150	PF	$\chi^2(4)$
IC 860	40 ^g	$206 \pm 79 / \geq 250$	PF,MTC	$\chi^2(4,1)$
M 83	31	56 ± 15	GF	R(2)
IR 15107+0724	40 ^g	189 ± 57	GF	R(2)
Arp 220	44	234 ± 52	GF	R(5,1)
Arp 220 G1	...	$136 \pm 18 / 223 \pm 30$	PF,MTC	R(4,1)
Arp 220 G2	...	$153 \pm 20 / 236 \pm 40$	PF,MTC	R(5,1)
NGC 6946	30	47 ± 8	GF	R(2)
NGC 6946 G1	...	25 ± 3	GF	R(2)
NGC 6946 G2	...	50 ± 10	GF	R(2)

^a Source name tags “G1”, “G2”, “G3”, and “G4” refer to Gaussian fit components from Table 3.

^b T_{dust} from Table 2.

^c Notes: GF \equiv good fit; PF \equiv poor fit; MTC \equiv multiple temperature components indicated; MVC \equiv multiple velocity components indicated.

^d Fit Types: R($\#$, $\#$) \equiv para- and ortho-NH₃ (if available) ratio fit using $\#$ transition ratios; $\chi^2(\#$, $\#$) \equiv χ^2 fit assuming $\#$ degrees of freedom for para-NH₃ and ortho-NH₃ (if available).

^e Average and range for all four components (see Section 5.3).

^f Fit over high density and column density range more constrained. See §7.1.

^g Assumed value.

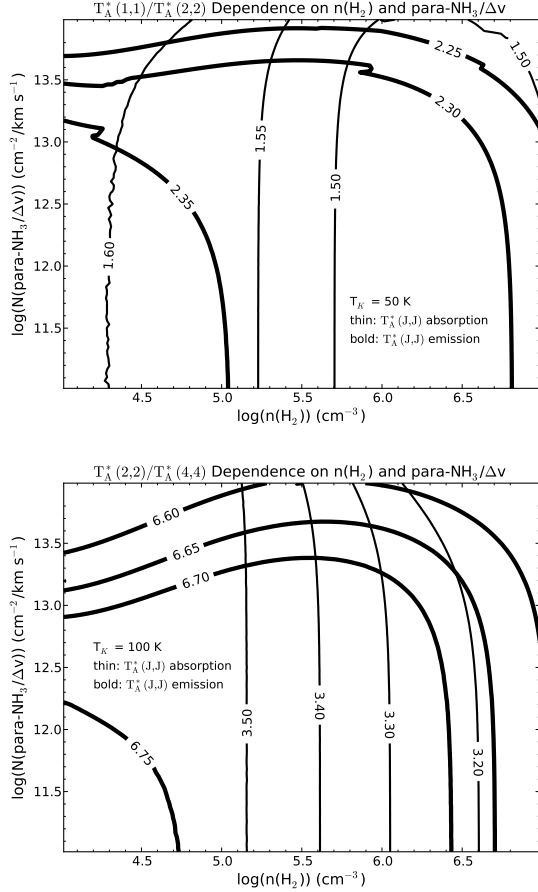


FIG. 12.— LVG model predictions of the NH_3 (1,1)/(2,2) (top panel) and (2,2)/(4,4) (bottom panel) transition ratios, for both emission and absorption, as functions of spatial density and NH_3 column density. Predicted transition ratios at representative kinetic temperatures, appropriate for the range of sensitivity for each transition ratio, are shown.

5.2. LVG Models with Background Continuum and Infrared Emission

5.2.1. Background Continuum Emission

For the five galaxies in our sample which exhibit NH_3 absorption a background continuum source must be added to our LVG model analysis. Even though we have estimates of the single-dish background continuum flux from our extragalactic NH_3 measurements (Table 3), in general we do not have a measurement of the 24 GHz continuum source size. We can estimate the likely continuum source size from other centimeter-wavelength continuum measurements. In §5.3 we list the relevant centimeter-wavelength continuum measurements for these five galaxies, all of which imply continuum source sizes of $\theta_s \lesssim 0.5$ arcsec. For 24 GHz continuum fluxes (Table 3) which range from 15 mJy (IR 15107+0724) to 140 mJy (Arp 220) within our $\theta_B \simeq 30$ arcsec beam, the continuum brightness temperatures from these five galaxies are estimated to be in the range 100 to 1000 K.

To further guide the allowable range of continuum brightness temperatures that we must consider, we note that four of the five NH_3 absorption galaxies are detected in the high-excitation NH_3 (7,7), (8,8), and/or

(9,9) transitions. Since for thermalized energy levels an absorption line is produced for $T_c \gtrsim T_{ex} \simeq T_K$, significant (7,7) absorption is produced only for $T_c \gtrsim 200$ K. For IR 15107+0724, where the highest excitation transition detected is the NH_3 (4,4) transition, significant absorption is produced for $T_c \gtrsim 100$ K.

To derive the kinetic temperature within these five NH_3 absorption galaxies we have constructed LVG models over similar ranges in $(n(\text{H}_2), N(\text{para-}\text{NH}_3)/\Delta v, T_K)$ as used to constrain our extragalactic NH_3 emission measurements and added blackbody background continuum sources with brightness temperatures of $T_c = 50, 100, 200, 300, 400$, and 500 K (Table 4). With the lower-limits to T_c noted above in mind, we investigated the behavior of the higher-excitation absorption transition ratios within these NH_3 LVG models. We find that there is a minimal ($\lesssim 10\%$) dependence of the derived kinetic temperature on the exact continuum brightness temperature chosen. Since the limitations of our NH_3 excitation rates restrict us to studies of gas with $T_K \lesssim 300$ K, we have adopted a uniform $T_c = 300$ K for all five of our NH_3 absorption galaxies. The kinetic temperatures listed in Table 5 are derived from fits to the LVG model cubes with $T_c = 300$ K. Note, though, as noted above, that fits to LVG model cubes with values of T_c ranging from 100 to 500 K do not produce appreciably different kinetic temperatures.

5.2.2. Embedded Infrared Emission

In NGC 253 and IC 342 we detect NH_3 (2,1) emission. As described in §2, Morris et al. (1973) showed that the level populations of the NH_3 (2,1) transition become inverted when $n(\text{H}_2) < 10^6 \text{ cm}^{-3}$ and $T_K = 50$ K (or $n(\text{H}_2) < 10^5 \text{ cm}^{-3}$ and $T_K = 100$ K, as shown in Figure 1) in the presence of a blackbody infrared radiation field. This condition results in detectable non-metastable NH_3 (2,1) emission under a wide range of physical conditions that our LVG models reproduce (see Figure 1). Higher-lying non-metastable ($J \neq K$) transitions also become inverted, but require higher infrared radiation fields and/or higher kinetic temperatures to produce the inverted populations.

One should also be concerned about the effects of the insertion of an embedded infrared source on the populations of the energy levels which comprise the NH_3 (1,1) and (2,2) transitions. Comparing LVG model predictions of the NH_3 (1,1) and (2,2) radiation temperatures with an undiluted (i.e. completely coupled to the source of molecular emission) 34 K blackbody infrared source (indicated with a superscript IR below) with those models which do not have infrared emission (see Table 4), we find that, for $n(\text{H}_2) = 10^4$ to 10^7 cm^{-3} :

- $\frac{T_R(1,1)}{T_R T_R(1,1)} = 0.65$ to 1.25 , increasing monotonically over the density range at all modelled T_K .
- $\frac{T_R(2,2)}{T_R T_R(2,2)} = 0.70$ to 1.10 , increasing monotonically over the density range for $T_K \gtrsim 50$ K
- $\frac{T_R(2,2)}{T_R T_R(2,2)} = 0.60$ to 0.90 , with minima at the extremes of the modelled density range and a maximum near $n(\text{H}_2) = 10^5 \text{ cm}^{-3}$, all for $T_K = 15$ to 50 K

Based on our LVG modelling, it appears that the kinetic temperature sensitive $\frac{T_R(1,1)}{T_R(2,2)}$ ratio, for a given (n, N, T_K) , is decreased by $\lesssim 30\%$ over the range of physical conditions considered when a moderate embedded infrared source is added.

Fundamentally, this behavior is due to the influence of the non-metastable excitation state on the metastable transitions. When the non-metastable transitions are driven into maser emission by the insertion of an infrared source, these non-metastable transitions occupy a larger fraction of the population distribution within NH_3 . This results in a lower intensity for the metastable transitions at the bottom of the K-ladders of NH_3 which has a stronger effect on lower-energy transitions. One can see this effect on the $\frac{T_R(1,1)}{T_R(2,2)}$ and $\frac{T_R(2,2)}{T_R(4,4)}$ transition ratios from the “cool component” of NGC 253NE and NGC 253SW shown in Figures 13 and 14, respectively. Effectively this imparts a slight spatial density dependence to the transition ratio. Furthermore, the density at which a transition ratio (i.e. $\frac{T_R(1,1)}{T_R(2,2)}$, $\frac{T_R(2,2)}{T_R(4,4)}$, $\frac{T_R(5,5)}{T_R(7,7)}$, etc.), begins to decrease is driven to higher densities as T_{IR} is increased. Quantitatively, for $T_{IR} = 100$ and 200 K, the kinetic temperature derived for a given NH_3 metastable transition ratio is decreased by ~ 15 and $\sim 30\%$ while the uncertainty associated with this kinetic temperature measurement is increased by a factor of two and three, respectively. Recall that our conservative error estimation incorporates any spatial density dependence to a kinetic temperature sensitive transition ratio.

5.3. Extragalactic Kinetic Temperature Fits and Comparison to Previous Ammonia Measurements

In the following we discuss our LVG model fits to our NH_3 measurements of the kinetic temperatures in our galaxy sample. We also compare our current extragalactic NH_3 detections and kinetic temperature measurements to existing measurements. Detailed summaries of existing dense-gas molecular line measurements toward these galaxies can be found in Mangum et al. (2008) and Mangum et al. (2013).

NGC 253: NH_3 measurements of the (1,1), (2,2), (3,3), (4,4), and (6,6) transitions toward this nearby starburst galaxy have been reported by several authors. Most of these measurements are able to spectrally, and in the case of imaging measurements spatially resolve the NH_3 emission toward NGC 253 into two distinct velocity components: a north-east (NE) component at $v \simeq 180 \text{ km s}^{-1}$ and a south-west (SW) component at $v \simeq 300 \text{ km s}^{-1}$.

The (1,1), (2,2), and (3,3) transitions have been detected by Takano et al. (2002) with spatial and spectral resolution $\theta_b = 71''$ and $\Delta v \simeq 20 \text{ km s}^{-1}$, respectively. The (4,4) transition was searched for but not detected, while the (2,2) transition was detected in only the 300 km s^{-1} component. Using only the (1,1), (2,2), and a limit to the (4,4) transition Takano et al. (2002) derive $T_K \lesssim 17$ and 37_{-6}^{+9} K for the 180 and 300 km s^{-1} components, respectively.

Mauersberger et al. (2003) measured the (1,1), (2,2), (3,3), (4,4), and (6,6) transitions at spatial and spectral resolution of $\theta_b = 38''$ and $\Delta v \simeq 15 \text{ km s}^{-1}$, respec-

tively. Using a rotation diagram analysis Mauersberger et al. (2003) derived $T_K = 142 \pm 14$ and 100 ± 3 K for the 180 and 300 km s^{-1} components, respectively. These relatively high temperatures are dominated by the emission from the (3,3) and (6,6) transitions, which has been shown to produce maser emission under a wide range of physical conditions in star formation regions (see Mangum & Wootten 1993). If the (3,3) and (6,6) transitions are excluded from their fit to T_K , the rotation temperatures derived are ~ 60 K for both velocity components.

Ott et al. (2005) imaged the (1,1), (2,2), (3,3), and (6,6) transitions at spatial and spectral resolution of $\theta_b = 30'' \times 5''$, position angle -12° , and $\Delta v \simeq 12 \text{ km s}^{-1}$, respectively. Six dense gas condensations were measured within a $\sim 30''$ region around the nucleus which generally fall into two groups: a NE group with $v \simeq 180 \text{ km s}^{-1}$ and a SW group with $v \simeq 300 \text{ km s}^{-1}$. These measurements associated for the first time the 180 and 300 km s^{-1} components noted previously and dense gas structures within NGC 253. Ott et al. (2005) also note NH_3 absorption in the (1,1), (2,2), and (6,6) transitions toward the central compact continuum source in NGC 253. Using an assumed ortho-to-para NH_3 ratio of unity, Ott et al. (2005) derive $T_K \simeq 140$ and 200 K toward the spatial components in the NE and SW of NGC 253, respectively. As was the case with the kinetic temperatures derived by Mauersberger et al. (2003) the high kinetic temperatures derived are largely dependent upon the intensities of the (3,3) and (6,6) transitions. Since Ott et al. (2005) note that the (3,3) transition is observed in emission toward the central compact continuum source position which produces NH_3 (1,1), (2,2), and (6,6) absorption, maser amplification of the (3,3) transition may be occurring. As noted above, both the (3,3) and (6,6) transitions are known to produce maser emission in star formation regions in our Galaxy (see Mangum & Wootten 1993). Using separate measurements of the NH_3 rotation temperature from the (1,1)/(2,2) (T_{12}) and (3,3)/(6,6) (T_{36}) transition ratios, Ott et al. (2005) derive NH_3 rotation temperatures of $T_{12} \simeq 37$ and 51 K and $T_{36} \simeq 108$ and 127 K, for the NE and SW components, respectively.

In an imaging measurement similar to that reported by Ott et al. (2005), Takano et al. (2005) imaged the (1,1), (2,2), and (3,3) transitions at spatial and spectral resolution of $\sim 4 \times 3''$ and $\Delta v \simeq 20 \text{ km s}^{-1}$, respectively. As with past NH_3 measurements the NE (180 km s^{-1}) and SW (300 km s^{-1}) spatial/spectral components were detected, along with NH_3 (1,1) absorption toward the central continuum source. Using only their (1,1) and (2,2) measurements Takano et al. (2005) derive $T_K \simeq 15$ to 28 K and $\simeq 20$ to 30 K toward the NE and SW components, respectively. The low kinetic temperatures derived likely reflect the low-excitation transitions employed in this study.

The $\sim 2.''5$ $\Delta v = 20 \text{ km s}^{-1}$ images of the NH_3 (3,3) emission from NGC 253 reported by Lebrón et al. (2011) arise from six GMC components located within a $40'' \times 5''$ structure with position angle $\sim 45^\circ$. The emission distribution measured is similar to previous high-resolution NH_3 studies of NGC 253.

Our $30''$ spatial resolution measurements of the para- NH_3 (1,1), (2,2), and (4,4) transitions and the ortho-

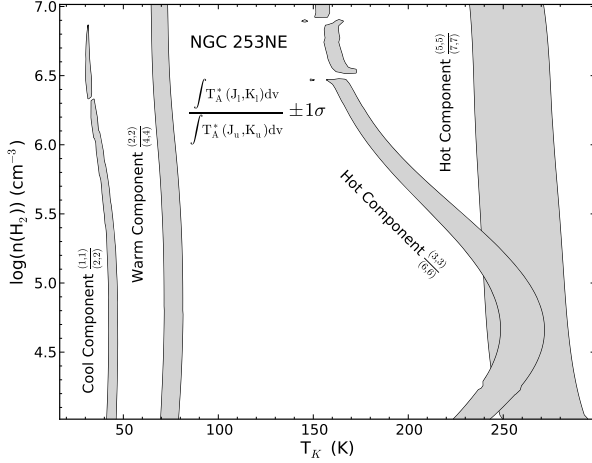


FIG. 13.— LVG model kinetic temperature fit to the $v_{opt} \approx 180 \text{ km s}^{-1}$ (NE) component of NGC 253. Shown as grey contours are the best-fit ratios at a representative $N(\text{species-NH}_3)/\Delta v = 10^{13.5} \text{ cm}^{-2}/\text{km s}^{-1}$ within one standard deviation for this spectral component using the (1,1)/(2,2), (2,2)/(4,4), (3,3)/(6,6), and (5,5)/(7,7) ratios which characterize the cool, warm, hot, and hot kinetic temperature components, respectively. The broken contours at $n(\text{H}_2) \gtrsim 10^{6.5} \text{ cm}^{-3}$ for the ortho- NH_3 (3,3)/(6,6) ratio are due to the onset of maser amplification in the (3,3) and (6,6) transitions.

NH_3 (3,3) and (6,6) transitions toward NGC 253 are in good agreement with many of the aspects of these previous studies. The addition of the (5,5), (7,7), (8,8), and (9,9) transitions allows us to better characterize the high temperature environment in this starburst galaxy. The HC_3N $J=3-2$ spectrum (Figure 2) was measured *gratis* as part of our NH_3 (7,7), (8,8), and (9,9) observing configuration. For both NH_3 and HC_3N we measure velocity components at ~ 180 and $\sim 300 \text{ km s}^{-1}$, consistent with the NE and SW components noted previously. Employing our LVG-based kinetic temperature analysis (§5.1) we obtain a poor fit to the kinetic temperature if an overall fit to both velocity components is made (see Table 5). T_K derived for each of the two velocity components produces fits which strongly suggest contributions due to multiple temperature components. Summarizing our T_K fits made toward NGC 253:

- *NE (180 km s⁻¹) Component:* This velocity component yielded a three-temperature fit: $T_K = 38 \pm 9 \text{ K} / 73 \pm 9 \text{ K} / > 150 \text{ K}$ using the $\frac{(1,1)}{(2,2)}$ (low-temperature component), $\frac{(2,2)}{(4,4)}$ (warm-temperature component), and combination of the para- NH_3 $\frac{(4,4)}{(5,5)}$, $\frac{(7,7)}{(8,8)}$, and ortho- NH_3 $\frac{(3,3)}{(6,6)}$, and $\frac{(6,6)}{(9,9)}$ (high-temperature component) transition ratios (Figure 13).
- *SW (300 km s⁻¹) Component:* This velocity component yielded a two-temperature fit: $T_K = 78 \pm 22 \text{ K} / > 150 \text{ K}$ using the combined $\frac{(1,1)}{(2,2)}$ and $\frac{(2,2)}{(4,4)}$ transition ratios (low-temperature component) and the combined para- NH_3 $\frac{(4,4)}{(5,5)}$, $\frac{(7,7)}{(8,8)}$, and ortho- NH_3 $\frac{(3,3)}{(6,6)}$, and $\frac{(6,6)}{(9,9)}$ transition ratios (high-

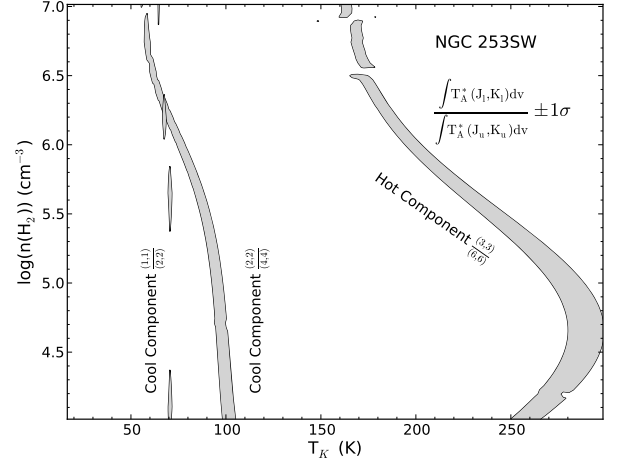


FIG. 14.— LVG model kinetic temperature fit to the $v_{opt} \approx 300 \text{ km s}^{-1}$ (SW) component of NGC 253. Shown as grey contours are the best-fit ratios at a representative $N(\text{species-NH}_3)/\Delta v = 10^{13.5} \text{ cm}^{-2}/\text{km s}^{-1}$ within one standard deviation for this spectral component using the (1,1)/(2,2), (2,2)/(4,4), and (3,3)/(6,6) ratios which characterize the cool, cool, and hot kinetic temperature components, respectively. Transition measurement ratios involving the higher-lying (5,5), (7,7), (8,8), and (9,9) transitions yield $T_K \gtrsim 300 \text{ K}$. The broken contours at $n(\text{H}_2) \gtrsim 10^{6.5} \text{ cm}^{-3}$ for the ortho- NH_3 (3,3)/(6,6) ratio are due to the onset of maser amplification in the (3,3) and (6,6) transitions. Broken contours for the para- NH_3 (1,1)/(2,2) cool component fit are due to the best-fit range being comparable to our LVG model cube kinetic temperature increment.

temperature component; Figure 14).

- *Whole Galaxy:* Due to the disparate kinetic temperatures derived for the NE and SW components, the kinetic temperature fit to the total galaxy NH_3 emission is poor. Taking an average of the kinetic temperature fits to the NE and SW components:

$$- T_K = 78 \pm 22 \text{ K} / > 150 \text{ K from levels lower and higher than (4,4), respectively.}$$

NGC 660: Our detections of the NH_3 (1,1) through (7,7) transitions in absorption are the first reported NH_3 measurements toward this polar ring galaxy. By far the most diverse and complicated NH_3 measurements in our galaxy sample, we present a detailed analysis of these remarkable spectra in Section 7.

NGC 891: This is a new detection of the NH_3 (1,1) transition toward this galaxy. With only a limit to the (2,2) and (4,4) intensities we derive only an upper limit to the kinetic temperature. High spatial resolution measurements of dense gas tracers in NGC 891 (see summary in Mangum et al. 2013) suggest that the molecular emission is mainly confined to a nuclear condensation that is $\sim 20'' \times 10''$ in extent.

Maffei 2: Takano et al. (2000) measured the NH_3 (1,1), (2,2), (3,3), and (4,4) transitions (did not detect the (4,4) transition) at $\theta_b \simeq 70''$ and $\Delta v \simeq 10 \text{ km s}^{-1}$. Henkel et al. (2000) measured the (1,1), (2,2), (3,3), and (4,4) transitions, while Mauersberger et al. (2003) measured the (6,6) transition toward this galaxy, all at $\theta_b \simeq 40''$

and $\Delta v \simeq 15 \text{ km s}^{-1}$. The NH_3 emission in all of these measurements is comprised of two velocity components at ~ -80 and $\sim +6 \text{ km s}^{-1}$. Takano et al. (2000) measure rotation temperatures $T_{\text{rot}} \simeq 30 \text{ K}$ over all emission velocities. Henkel et al. (2000) derive $T_{\text{rot}} = 85 \pm 5 \text{ K}$ for the -80 km s^{-1} component and $T_{\text{rot}} = 55 \pm 10 \text{ K}$ for the $+6 \text{ km s}^{-1}$ component using only the (1,1), (2,2), and (3,3) transitions (deconvolution of the (4,4) transition into two velocity components was considered tentative by Henkel et al. (2000)). Combining their NH_3 (6,6) measurement to the Henkel et al. (2000) measurements, Mauersberger et al. (2003) derive $T_{\text{rot}} = 48 \pm 15 \text{ K}$ using NH_3 (1,1) and (2,2) and $T_{\text{rot}} = 132 \pm 12 \text{ K}$ using NH_3 (3,3) and (6,6) over both velocity components.

The $\theta_b \sim 3.''5$ $\Delta v = 20 \text{ km s}^{-1}$ images of the NH_3 (1,1) and (2,2) emission from Maffei 2 reported by Lebrón et al. (2011) arise from four main GMC components grouped into three velocity ranges near -80 , 0 , and $+20 \text{ km s}^{-1}$. The overall NH_3 emission is located within a $\sim 20'' \times 5''$ structure with position angle $\sim 30^\circ$. In addition to the emission detected from all four GMCs, NH_3 (2,2) absorption from “peak B” ($v_{\text{hel}} \simeq -85 \text{ km s}^{-1}$) against the centimeter continuum emission peak in Maffei 2 was noted. Derived T_{rot} for the four GMCs imaged range from 25 – 50 K .

Our measurements of the NH_3 (1,1), (2,2), and (4,4) transitions toward Maffei 2 reflect the same two-velocity component structure previously noted. Using our NH_3 (1,1), (2,2), and (4,4) measurements, both the -80 km s^{-1} (Maffei 2 G1) and $+20 \text{ km s}^{-1}$ (Maffei 2 G2) velocity components deconvolve into low-temperature ($T_K \simeq 40 \text{ K}$) and high-temperature ($T_K \simeq 80 \text{ K}$) components. The kinetic temperature fits to both velocity components is poor due to this multiple-temperature component structure.

NGC 1365: The NH_3 emission from this galaxy appears to emanate from two velocity components; at $v_{\text{hel}} \sim 1575$ and $\sim 1730 \text{ km s}^{-1}$. The $\text{H}_2\text{CO } 1_{10}-1_{11}$ absorption spectrum reported by Mangum et al. (2013) is suggestive of this same two-velocity component structure. The quality of the kinetic temperature fit for this galaxy is good, well constrained by the NH_3 (1,1) and (2,2) transitions detected towards both velocity components. The velocity component near $v_{\text{hel}} \simeq 1575 \text{ km s}^{-1}$ (NGC 1365 G1) appears to be significantly warmer ($T_K \simeq 100 \text{ K}$) than the velocity component near $v_{\text{hel}} \simeq 1730 \text{ km s}^{-1}$ (NGC 1365 G2; $T_K \simeq 30 \text{ K}$). Figure 15 shows the LVG model fit to the kinetic temperature in this galaxy. We are not aware of any previous measurements of NH_3 toward this galaxy.

IC 342: The NH_3 emission from this galaxy, the first extragalactic object ever detected in NH_3 (Martin & Ho 1979), appears to originate in two velocity components; at $v_{\text{hel}} \simeq 25$ (G1) and $\simeq 50 \text{ km s}^{-1}$ (G2). The NH_3 (1,1) through (9,9) transition measurements reported in Mauersberger et al. (2003) and the $\text{H}_2\text{CO } 1_{10}-1_{11}$ and $2_{11}-2_{12}$ absorption spectra reported by Mangum et al. (2008, 2013) originate from a single velocity component with $v_{\text{hel}} \simeq 25 \text{ km s}^{-1}$. Mauersberger et al. (2003) derive NH_3 rotational temperatures of $\sim 50 \text{ K}$ (from their (1,1) through (3,3) measurements) and $\sim 400 \text{ K}$ (from their (5,5) through (9,9) measurements), suggesting contribu-

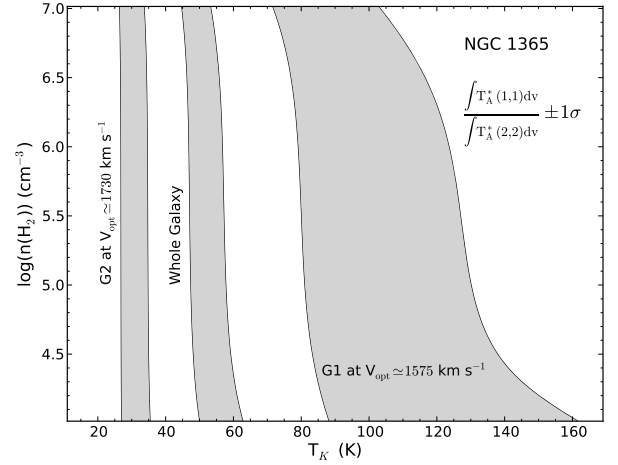


FIG. 15.— LVG model kinetic temperature fit to the individual velocity components in NGC 1365. Shown as grey contours are the best-fit ratios within one standard deviation for the two velocity components of NGC 1365 and for the galaxy as a whole.

tions from warm and hot dense gas.

The $\theta_b \sim 3.''5$ $\Delta v = 20 \text{ km s}^{-1}$ images of the NH_3 (1,1) and (2,2) emission from IC 342 reported by Lebrón et al. (2011) and the $\theta_b \sim 6''$ $\Delta v = 9 \text{ km s}^{-1}$ images of the NH_3 (6,6) emission from IC 342 reported by Montero-Castaño et al. (2006) both identified four of the five giant molecular cloud (GMC) complexes previously noted by Downes et al. (1992) and Meier & Turner (2001). In their $\sim 2''$ $\Delta v = 10 \text{ km s}^{-1}$ images of the $\text{HC}_3\text{N } J=5-4$ and $J=16-15$ emission from IC 342 Meier et al. (2011) identified all five of these GMC complexes. The central velocities of these GMC complexes (identified as GMC A through E) fall into three groups; a complex with $v_{\text{hel}} \simeq 12 \text{ km s}^{-1}$ (GMC E, comprising the SW spiral arm of IC 342), two complexes with $v_{\text{hel}} \simeq 25 \text{ km s}^{-1}$ (GMC A and B, comprising the nuclear star forming region and central bar of IC 342), and two complexes with $v_{\text{hel}} \simeq 50 \text{ km s}^{-1}$ (GMC C and D, comprising the NE spiral arm of IC 342). The NH_3 velocity component G1 ($v_{\text{hel}} \simeq 25 \text{ km s}^{-1}$) corresponds to the GMC complexes A and B, while G2 ($v_{\text{hel}} \simeq 50 \text{ km s}^{-1}$) corresponds to the GMC complexes C and D. Meier et al. (2011) and Montero-Castaño et al. (2006) note that the $\text{HC}_3\text{N } J=16-15$ and NH_3 (6,6) transitions, respectively, are most intense toward GMC complex C, which corresponds to the NH_3 velocity component G2 near $v_{\text{hel}} \simeq 50 \text{ km s}^{-1}$.

Lebrón et al. (2011) derive $T_{\text{rot}} \simeq 25$ – 35 K from their NH_3 (1,1) and (2,2) images, limited by the low excitation of these two NH_3 transitions. The high-excitation NH_3 (6,6) ($E_u = 408 \text{ K}$) measurements reported by Montero-Castaño et al. (2006) suggest higher kinetic temperatures within both of the velocity components within this galaxy. Using their images of the $\text{HC}_3\text{N } J=5-4$, $10-9$ (Meier & Turner 2005), and $16-15$ emission, Meier et al. (2011) constrain LVG models of the spatial density and kinetic temperature toward the GMC complexes in this galaxy. They derive kinetic temperatures in the range 30 – 70 K and spatial densities in the range 10^3 – 10^5 cm^{-3} . The lower spatial densities in these LVG models correspond to higher kinetic temperatures, and vice-versa,

which is a reflection of the degeneracy within LVG models which attempt to derive both kinetic temperature and spatial density from molecular transitions with coupled sensitivity to both physical parameters.

Our NH_3 -constrained derivations of the kinetic temperatures from the two velocity components G1 and G2 point to the existence of kinetic temperature gradients or multiple temperature components. The $v_{\text{hel}} \simeq 25 \text{ km s}^{-1}$ (G1, or nuclear star forming region) component clearly possesses multiple kinetic temperature components. Individual NH_3 transition ratios result in the following LVG model derived kinetic temperatures for this velocity component:

- $T_K = 24 \pm 7 \text{ K}$ using (1,1)/(2,2)
- $T_K = 115 \pm 17 \text{ K}$ using (2,2)/(4,4)
- $T_K > 188 \text{ K}$ using (4,4)/(5,5)
- $T_K > 141 \text{ K}$ using (3,3)/(6,6)

suggesting that there are at least three temperature components comprising the G1 velocity component of IC 342. The $v_{\text{hel}} \simeq 50 \text{ km s}^{-1}$ (G2, or NE spiral arm) component also appears to possess multiple kinetic temperature components. Individual NH_3 transition ratios result in the following LVG model derived kinetic temperatures for this velocity component:

- $T_K > 90 \text{ K}$ using (1,1)/(2,2)
- $T_K = 75 \pm 14 \text{ K}$ using (2,2)/(4,4)
- $T_K > 300 \text{ K}$ using (4,4)/(5,5)
- $T_K > 186 \text{ K}$ using (3,3)/(6,6)

suggesting that there are at least two temperature components comprising the G2 velocity component of IC 342. Note also that the G2 velocity component is a source of weak NH_3 (2,1) emission, suggesting intense infrared emission associated with this component. This fact, coupled with the lack of low-temperature gas in the G2 component suggests a more energetic star formation event in the NE spiral arm region of IC 342 than that found in the nuclear region of this galaxy.

M 82SW: In addition to the central position in M 82 (a non-detection), we searched for NH_3 emission at a position offset of $(-12, -4)$ arcsec from the nominal M 82 position known to be a source of NH_3 emission (Weiß et al. 2001, identified as the “southwestern molecular lobe”). The $\theta_b \simeq 40''$ and $\Delta v \simeq 16 \text{ km s}^{-1}$ measurements of the (1,1), (2,2), (3,3), and (4,4) transitions by Weiß et al. (2001) resulted in a kinetic temperature of $\simeq 60 \text{ K}$ based on a rotation diagram analysis of their (1,1), (2,2), and (3,3) spectra (they did not detect the (4,4) transition). The LVG model fit to our NH_3 (1,1) and (2,2) spectra result in a similar kinetic temperature (Figure 16). High spatial resolution measurements of dense gas tracers in M 82 (see summary in Mangum et al. 2013) suggest that the molecular emission extends over a $40'' \times 15''$ disk-like structure.

NGC 3079: The NH_3 absorption toward NGC 3079 possesses the same two-component spectral structure as that

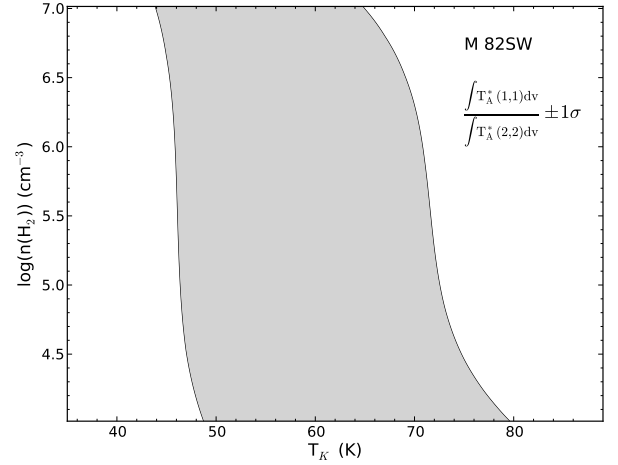


FIG. 16.— LVG model kinetic temperature fit to M 82SW. Shown as grey contours is the best-fit ratio within one standard deviation for the NH_3 (1,1) and (2,2) emission toward M 82SW.

observed in the $\text{H}_2\text{CO } 2_{11} - 2_{12}$ measurements reported in Mangum et al. (2013). The $\text{H}_2\text{CO } 1_{10} - 1_{11}$ measurements reported in Mangum et al. (2008, 2013) also have the same velocity structure as that observed in our NH_3 measurements, with the exception that there is a tentative, weak $\text{H}_2\text{CO } 1_{10} - 1_{11}$ absorption component at $v_{\text{hel}} \simeq 1500 \text{ km s}^{-1}$ that is just outside the bandwidth of our NH_3 measurements. We are not aware of any previous NH_3 measurements toward this galaxy. The background continuum source in NGC 3079 is estimated to be $\lesssim 0.5''$ in extent (see Duric et al. 1983; Kukula et al. 1995).

Unexplained is the non-detection of NH_3 (3,3) toward this galaxy, even though we detect the higher-excitation (6,6) and (9,9) transitions. Attempts were made to detect NH_3 (3,3) using four different correlator configurations spanning four observing runs during the time period 2011/10/30 through 2011/11/04, one of which was tuned exclusively to the (3,3) transition. During two of the four observing runs NH_3 (3,3) was detected in three other targets; the Galactic molecular cloud W3(OH) and starburst galaxies NGC 253 and NGC 660. These checks of the observing setup involving NH_3 (3,3) appear to eliminate faulty observing configuration as the reason for the non-detection of NH_3 (3,3) in NGC 3079.

With the exception of ad-hoc and improbable explanations which involve inconsistent source size distributions between NH_3 (3,3) and all other para- and ortho- NH_3 transitions, our non-detection of NH_3 (3,3) toward NGC 3079 is difficult to explain. One possibility is the existence of a separate physical component within NGC 3079 which has physical conditions which result in NH_3 (3,3) maser emission which cancels any NH_3 (3,3) absorption from the physical structures which also produce absorption in the other NH_3 transitions. To study this possibility we have investigated the optical depth values produced by our LVG models of the NH_3 (3,3), (6,6), and (9,9) transitions.

As there is only a minimal dependence of the absolute NH_3 (3,3), (6,6), and (9,9) optical depths on the model input continuum background temperature T_c , we have

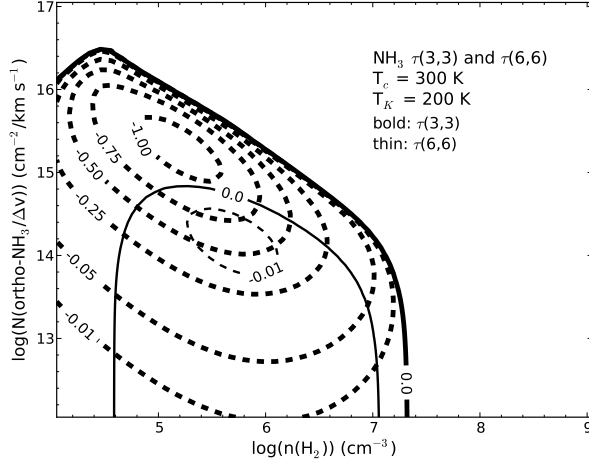


FIG. 17.— LVG model predictions of NH_3 (3,3) and (6,6) maser ($\tau < 0$) emission for an assumed $T_c = 300$ K and $T_K = 200$ K.

restricted our optical depth comparison as a function of spatial density, NH_3 column density, and kinetic temperature to $T_c = 300$ K. For this assumed background continuum temperature, our LVG models predict:

- $\tau(3,3) \leq 0$ for $T_K \gtrsim 25$ K and a range of $n(\text{H}_2)$ and $N(\text{ortho-NH}_3)/\Delta v$ which peaks at $\tau(3,3) \simeq -1.0$ near $n(\text{H}_2) \simeq 10^{5.25} \text{ cm}^{-3}$ and $N(\text{ortho-NH}_3) \simeq 10^{15.5} \text{ cm}^{-2}/\text{km s}^{-1}$ and widens in (n, N) as T_K increases.
- $\tau(6,6) \leq 0$ for $T_K \gtrsim 100$ K and a range of $n(\text{H}_2)$ and $N(\text{ortho-NH}_3)/\Delta v$ which peaks at $\tau(6,6) \simeq -0.01$ near $n(\text{H}_2) \simeq 10^{5.75} \text{ cm}^{-3}$ and $N(\text{ortho-NH}_3) \simeq 10^{14.25} \text{ cm}^{-2}/\text{km s}^{-1}$ and, like $\tau(3,3)$, widens in (n, N) as T_K increases.
- $\tau(9,9)$ is never less than 0 over the range of physical conditions modelled.

Figure 17 shows the LVG modelled optical depth when $\tau \leq 0$ for the NH_3 (3,3) and (6,6) transitions at a representative T_K of 200 K (appropriate for NGC 3079). As the LVG model predictions suggest that it is relatively easy to drive the NH_3 (3,3) transition into maser emission, a model which produces cancelling NH_3 (3,3) emission and absorption from two spectral components, with the same velocity and line width, along the line-of-sight seems plausible. Furthermore, this scenario is lent some credence by the fact that the $\text{H}_2\text{CO } 1_{10} - 1_{11}$ transition profile presented in Mangum et al. (2013) suggests both emission and absorption contributions. Low spatial densities ($n(\text{H}_2) \lesssim 10^{5.5} \text{ cm}^{-3}$) result in $\text{H}_2\text{CO } 1_{10} - 1_{11}$ absorption, while higher spatial densities ($n(\text{H}_2) \gtrsim 10^{5.5} \text{ cm}^{-3}$) result in $\text{H}_2\text{CO } 1_{10} - 1_{11}$ emission.

Our NH_3 (1,1) through (9,9) spectra provide only lower limits of 100 and 150 K to the kinetic temperature in both of the $v_{\text{opt}} \simeq 1020 \text{ km s}^{-1}$ (NGC 3079G1) and 1115 km s^{-1} (NGC 3079G2) velocity components. The highest-excitation para- NH_3 ((5,5)/(7,7)) and ortho- NH_3 ((6,6)/(9,9)) ratios imply $T_K \gtrsim 230$ K for both velocity components.

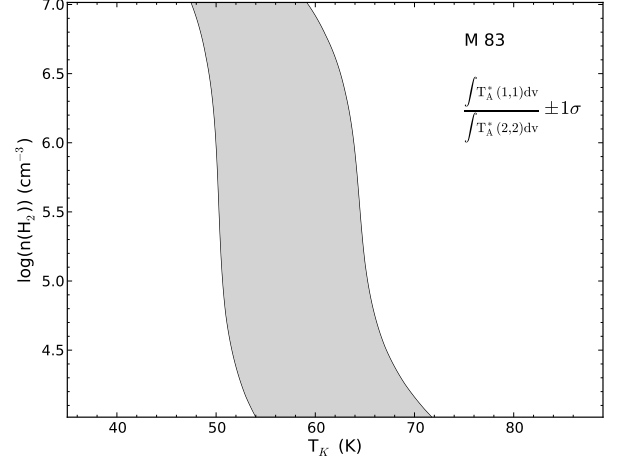


FIG. 18.— LVG model kinetic temperature fit to M83. Shown as grey contours is the best-fit ratio within one standard deviation for the NH_3 (1,1) and (2,2) emission toward M83.

IC 860: The NH_3 absorption in this galaxy, which is to our knowledge the first reported, corresponds spectrally to the $\text{H}_2\text{CO } 1_{10} - 1_{11}$ emission and $2_{11} - 2_{12}$ absorption components (Mangum et al. 2013). The background continuum source size is estimated to be $\lesssim 0.5''$ (see Condon et al. 1990, and references therein). The LVG-derived kinetic temperature fit to our ortho- and para- NH_3 (1,1) through (7,7) measurements is poorly constrained due to the influence of multiple high-temperature components. The (5,5)/(7,7) ratio implies a kinetic temperature $\gtrsim 250$ K, while all other line ratios are best described by T_K in the range 206 ± 79 K.

M 83: The quality of the kinetic temperature fit for this galaxy is good, well constrained by the NH_3 (1,1) and (2,2) transitions detected (Figure 18). We are not aware of any previous measurements of NH_3 toward this galaxy. High spatial resolution measurements of dense gas tracers in M83 (see summary in Mangum et al. 2013) suggest that the molecular emission extends over a $45'' \times 15''$ structure.

IR 15107+0724: The NH_3 (1,1), (2,2), and (4,4) absorption spectra measured toward this galaxy, representing new discoveries of NH_3 , have the same velocity structure measured in the $\text{H}_2\text{CO } 1_{10} - 1_{11}$ and $2_{11} - 2_{12}$ transitions reported in Mangum et al. (2013). Due to the relative weakness of the NH_3 (4,4) absorption ($\sim 4.4\sigma$ in integrated intensity), the kinetic temperature derived is based on the NH_3 (1,1) and (2,2) measurements toward this galaxy. The background continuum source size is estimated to be $\lesssim 1''$ (see Condon et al. 1990, and references therein).

Arp 220/IC 4553: Mangum et al. (2008, 2013) report detections of the $\text{H}_2\text{CO } 1_{10} - 1_{11}$ transition in emission and the $2_{11} - 2_{12}$ transition in absorption. These H_2CO measurements exhibit a primarily two-velocity component structure with $v_{\text{hel}} \sim 5350$ and 5500 km s^{-1} , with a tentative detection of a third component near $v_{\text{hel}} \sim 5600 \text{ km s}^{-1}$. This primarily two-component velocity structure has been noted in previous studies of the high-density emission from Arp 220 (HCN , HCO^+ ,

HNC; see Greve et al. 2009), whereby the $\sim 5350 \text{ km s}^{-1}$ component has been associated with the western nucleus of the merger, while the eastern nucleus produces the $\sim 5500 \text{ km s}^{-1}$ velocity component. The Greve et al. (2009) analysis of these two velocity components suggests that the western nucleus possesses a lower spatial density than the eastern nucleus, but our H_2CO measurements do not necessarily support this interpretation (Mangum et al. 2008, 2013). The background continuum source size is estimated to be $\lesssim 0.6''$ (see Ott et al. 2011, and references therein).

Our NH_3 measurements replicate the two-velocity component structure noted in previous studies (see Table 3 and Figure 10). The NH_3 (1,1) through (8,8) metastable ($J=K$) transitions all exhibit $v_{\text{hel}} \sim 5350$ and 5500 km s^{-1} components. The non-metastable NH_3 (10,9) (in the same spectrum as the NH_3 (4,4) transition; see Figure 10) and $\text{OH } ^2\Pi_{3/2} J=9/2 F=5-5$ transition (in the same spectrum as NH_3 (3,3); see Figure 10) only appear to have $v_{\text{hel}} \sim 5500 \text{ km s}^{-1}$ components. A broad ($\Delta v \simeq 530 \text{ km s}^{-1}$) low-velocity component with $v_{\text{hel}} \simeq 5200 \text{ km s}^{-1}$ is apparent in our NH_3 (1,1)/(2,2) spectrum. This component might be a broad blue-shifted wing of a dense molecular outflow.

To investigate the possible sources of this broad low-velocity spectral component in Arp 220, we consider two possibilities:

- *There is an additional molecular or atomic species that produces this spectral feature.* A search of molecular and atomic transition frequency lists indicates that only the $\text{H}109\epsilon$ recombination line at 23743.83 MHz , which would correspond to emission from the G2 ($v_{\text{hel}} \simeq 5500 \text{ km s}^{-1}$) component in Arp 220, could produce the additional broad, low-velocity component we measure. Radio recombination transitions have been detected toward Arp 220 (Mangum et al. 2013; Anantharamaiah et al. 2000), but only from the lower-excitation $\text{H}\alpha$ transitions. Furthermore, these $\text{H}\alpha$ recombination transitions have FWHM line widths $\sim 200 \text{ km s}^{-1}$, much narrower than the FWHM $\sim 530 \text{ km s}^{-1}$ H_2CO component we measure.
- *The (1,1) transition is anomalously weak, or that the (2,2) transition is anomalously broad and intense.* Ott et al. (2011) proposed that the lower intensity of the NH_3 (1,1) transition was due to an undetected cold ($T_K \lesssim 20 \text{ K}$) NH_3 emission component that is not spatially aligned with the background continuum source in Arp 220, but is spectrally overlapped with the main NH_3 (2,2) components. An alternative explanation is that the NH_3 (2,2) transition is anomalously broadened and intensified by a third velocity component. This scenario seems to be supported by the evidence for a broad velocity component shifted by approximately 200 km s^{-1} relative to the nominal $v_{\text{hel}} = 5290$ and 5460 km s^{-1} velocity components in our NH_3 (1,1) and (2,2) spectrum (Figure 10). Furthermore, *Herschel*/PACS spectroscopic measurements of OH ($163 \mu\text{m}$), $[\text{O I}]$ ($145 \mu\text{m}$), and H_2O ($82\text{--}90 \mu\text{m}$) toward Arp 220 point to a blueshifted $550\text{--}1000 \text{ km s}^{-1}$ wide ve-

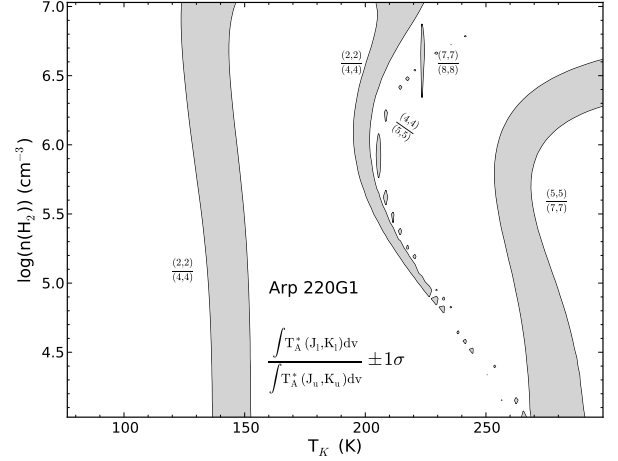


FIG. 19.— LVG model kinetic temperature fit to the G1 ($v_{\text{opt}} \simeq 5350 \text{ km s}^{-1}$) component of Arp 220. Shown as grey contours are the best-fit ratios within one standard deviation for the (2,2) through (8,8) transitions.

locity component offset by $\sim 400 \text{ km s}^{-1}$ from the systemic velocity of this merger system (González-Alfonso et al. 2012). These *Herschel*/PACS observations appear to be consistent with an interpretation whereby our GBT NH_3 (1,1) and (2,2) measurements possess a blueshifted wide-linewidth component which can be interpreted as evidence for a dense outflow in Arp 220.

A global single-temperature fit to either velocity component or the total Arp 220 NH_3 emission fails due to the apparent existence of kinetic temperature structure. Para- NH_3 transition ratio fits to the $v_{\text{hel}} \sim 5350 \text{ km s}^{-1}$ (Arp 220G1) component result in an apparent two-temperature structure: $T_K = 136 \pm 18 \text{ K}$ derived from NH_3 (2,2) and (4,4), $T_K = 223 \pm 30 \text{ K}$ derived from all five para- NH_3 transitions (Figure 19). For the $v_{\text{hel}} \sim 5500 \text{ km s}^{-1}$ (Arp 220G2) component a two-temperature structure is also observed: $T_K = 153 \pm 20 \text{ K}$, derived from NH_3 (1,1) and (2,2), $T_K = 236 \pm 40 \text{ K}$, derived from NH_3 (4,4) through (8,8). Fits to the ortho- NH_3 (3,3) and (6,6) ratio proved to be very complex, yielding a good fit only for $T_K > 90 \text{ K}$ and $156 \pm 15 \text{ K}$ for Arp 220G1 and G2, respectively, over $n(\text{H}_2) > 10^{6.7} \text{ cm}^{-3}$ and $N < 10^{16.75} \text{ cm}^{-2} / \text{km s}^{-1}$ for G1 and $n(\text{H}_2) \simeq 10^{6.4} \text{ cm}^{-3}$ and $N \gtrsim 10^{16.9} \text{ cm}^{-2} / \text{km s}^{-1}$ for G2. As noted in the discussion about the non-detection of NH_3 (3,3) absorption toward NGC 3079, the ortho- NH_3 (3,3) and (6,6) transitions arise at a wide range of spatial densities, NH_3 column densities, and kinetic temperatures. As Arp 220 is known to be a spatially complex source, including spatial densities which are apparently high enough to produce $\text{H}_2\text{CO } 1_{10} - 1_{11}$ emission (Mangum et al. 2013), it seems plausible to associate the complex and nearly uninterpretable NH_3 (3,3) and (6,6) absorption from this merger as being due to spatial and kinetic structure.

The kinetic temperature derived from our GBT NH_3 (1,1) through (8,8) measurements is consistent, though somewhat larger, than the rotation diagram analysis of the kinetic temperature of $186 \pm 55 \text{ K}$ derived from ATCA measurements of the (2,2) through (6,6) transitions of

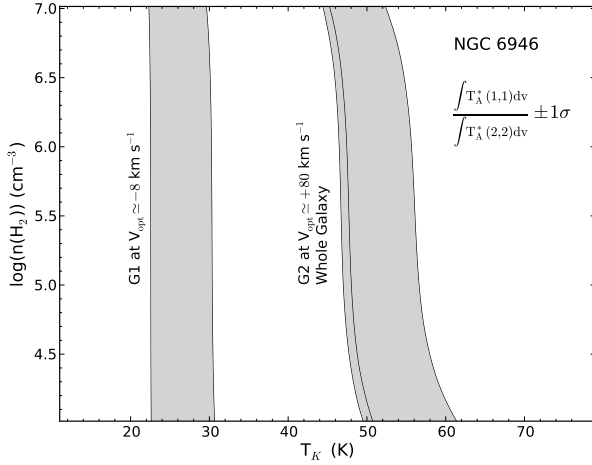


FIG. 20.— LVG model kinetic temperature fit to the individual velocity components in NGC 6946. Shown as grey contours are the best-fit ratio within one standard deviation for the two velocity components of NGC 6946 and for the galaxy as a whole.

para- and ortho-NH₃ presented by Ott et al. (2011). Clearly the inclusion of higher excitation NH₃ transitions in the present analysis has driven the derived kinetic temperature higher.

NGC 6946: Mangum et al. (2008, 2013) report detections of the H₂CO 1₁₀ – 1₁₁ and 2₁₁ – 2₁₂ transitions in absorption toward this galaxy, where a two-velocity component structure was noted with $v_{hel} \simeq -8$ and $\simeq +80$ km s⁻¹. Our measurements of the NH₃ (1,1) and (2,2) transitions are consistent with this two-velocity component structure. The quality of the kinetic temperature fits to both velocity components for this galaxy are good, well constrained by the NH₃ (1,1) and (2,2) transitions detected, suggesting that the +80 km s⁻¹ component (NGC 6946 G2) is significantly warmer than the -8 km s⁻¹ component (NGC 6946 G1; see Figure 20). We are not aware of any previous measurements of NH₃ toward this galaxy. High spatial resolution measurements of dense gas tracers in NGC 6946 (see summary in Mangum et al. 2013) suggest that the molecular emission emanates from two compact components: a compact nuclear source of size $\sim 2''$ and a “nuclear spiral” which is $\sim 5'' \times 10''$ in extent.

Non-Detected Galaxies: Ten galaxies were not detected in NH₃ to single-channel ($\Delta v \simeq 5 - 10$ km s⁻¹) RMS levels of ~ 0.8 to 2 mK (see Table 3). Six of these ten galaxies: NGC 598, IR 01418+1651, NGC 3690, NGC 4214, NGC 4418, and NGC 6951, are not known to be dense gas emission sources. Two galaxies: NGC 598 and IR 01418+1651, were also not detected in the H₂CO survey of Mangum et al. (2008, 2013). Mrk 231 is known to be a source of dense gas emission (e.g. Aalto et al. 2012), but was not included in this H₂CO survey. The remaining three galaxies: NGC 1144, NGC 2146, and NGC 3628, are all detected in H₂CO 1₁₀ – 1₁₁ absorption, and with the exception of NGC 1144 also detected in 2₁₁ – 2₁₂ absorption (Mangum et al. 2013). All three galaxies are also HCN emission sources (Gao & Solomon 2004a). The measured H₂CO 1₁₀ – 1₁₁ intensities of NGC 1144, NGC 2146, and NGC 3628 are

not particularly large (peak $T_A^* \simeq -1$ to -8 mK), implying H₂CO column densities $N(\text{ortho-H}_2\text{CO})/\Delta v \simeq 10^{11}$ cm⁻² km s⁻¹, which are on the low end of the range of H₂CO-detected galaxies (Mangum et al. 2013). Although we might have hoped to detect weak NH₃ emission from these three galaxies, the fact that we did not detect NH₃ in these galaxies is not a surprise.

6. DETECTION OF OH ²Π_{3/2} J=9/2 ABSORPTION TOWARD ARP 220

Ott et al. (2011) reported a tentative detection of the F=4 – 4 and F=5 – 5 magnetic hyperfine structure transitions from the ²Π_{3/2} J=9/2 lambda doublet state of OH toward Arp 220. The Ott et al. (2011) detection of this OH doublet, which lies at an energy above ground of ~ 512 K, was considered tentative as they detected an absorption line at approximately the correct frequency in their Australia Telescope Compact Array (ATCA) spectra, but not in their GBT spectra measuring the same frequency. Our measurements of the NH₃ (3,3) transition toward Arp 220 include the frequency range occupied by the OH ²Π_{3/2} J=9/2 doublet (Figure 10). The absorption component located $\sim +650$ km s⁻¹ from the NH₃ (3,3) absorption line is best-fit to a $v_{opt} = 5464.1 \pm 13.2$ km s⁻¹ (Table 3) at the rest frequency of the OH ²Π_{3/2} J=9/2 F=5 – 5 transition (23826.6211 MHz; see Table 1). The F=4 – 4 component would be located $\sim +150$ km s⁻¹ (~ 10 MHz) from the F=5 – 5 transition. Examination of the NH₃ (3,3) spectrum in Figure 10 suggests that the F=4 – 4 component may also have been detected, but that the purported OH ²Π_{3/2} J=9/2 doublet absorption is dominated by the F=5 – 5 transition. Note that absorption in the far infrared rotational OH transitions from both the ²Π_{3/2} and ²Π_{1/2} states with upper state energies as high as ~ 900 K have been measured toward Arp 220 (González-Alfonso et al. 2012). A significant contributor to this high-excitation OH absorption appears to originate from a dense outflow component in Arp 220. Other hyperfine transitions from within rotationally excited OH doublet states within both the ²Π_{3/2} and the ²Π_{1/2} ladders have recently been detected toward Arp 220 by Salter et al. (2008) with the Arecibo 305 meter telescope.

7. THE REMARKABLE NH₃ ABSORPTION TOWARD NGC 660

NGC 660, perhaps best known for its exquisite crossing dust lanes, is a nearly edge-on SB(s)a LINER galaxy with a polar ring. The radio continuum images presented by Condon (1980) and Condon et al. (1982, 1990) show bright, compact emission from the nucleus of NGC 660. The nuclear region harbors a continuum source which has been interpreted as a ring of high density and compact star formation regions (Carral et al. 1990). There is no observed central, compact core to indicate activity from an AGN and no X-ray counterpart to the nucleus (Dudik et al. 2005). The relatively high infrared luminosity ($10^{10.3} L_\odot$), optical LINER spectrum, and indications that star formation processes dominate the contribution to the radio flux establish NGC 660 as a moderate starburst. H₂CO (Mangum et al. 2008, 2013), NH₃ (this work), OH, and HI (Baan et al. 1992a) have all been

TABLE 6
CONTINUUM MEASUREMENTS OF NGC 660

ν (MHz)	S_ν (mJy)	θ_b	Reference
408	830 ± 70	$2'30''$	Large et al. (1981)
2400	255 ± 13	$2'42''$	Dressel & Condon (1978)
4850	187 ± 26	$3'30''$	Gregory & Condon (1991)
4850	184 ± 28	$3'30''$	Becker et al. (1991)
5000	156 ± 18	$2'42''$	Sramek (1975)

observed in absorption against this compact continuum source.

An extensive study of NGC 660 has been carried out by van Driel et al. (1995). The disk is seen almost edge-on with inclination $i \sim 70^\circ$ at a position angle of $PA \approx 45^\circ$. The polar ring is inclined on average $i \approx 55^\circ$ at $PA \approx 170^\circ$. A two component dust model with $T_d \approx 19$ K and $T_d \approx 50$ K has been fit to the millimeter/submillimeter dust emission from NGC 660 (Chini & Kruegel 1993), while a single temperature dust model yields $T_d \approx 37$ K.

High spatial resolution imaging of the HI and OH absorption from the nuclear region of NGC 660 have been carried out by Baan et al. (1992b). $H\alpha$ images show active star formation and HII regions throughout the polar ring (van Driel et al. 1995). The rotation curve, mass of the polar ring ($M_{ring} \sim 15.5 \times 10^9 M_\odot$), and mass of the disk ($M_{disk} \sim 19.4 \times 10^9 M_\odot$) have been derived from HI observations (van Driel et al. 1995). An outflow has been observed normal to the disk axis (Heckman et al. 2000).

Radio continuum images of the nuclear region of NGC 660 show compact ($\theta \lesssim 6''$) morphological components which can be interpreted as an edge-on ring or linear jet in the northeast-southwest direction. Without a clearly identifiable radio core, indicative of an AGN, large complexes of high-density star formation regions are proposed as the source of the compact radio emission (Carral et al. 1990). The optical nucleus is located $\sim 3''$ south of the strongest 15 GHz continuum peak (Filho et al. 2002).

To further understand the radio continuum emission source we have compiled measurements of the radio continuum flux from the literature to calculate the spectral index in the frequency range 408 MHz to 5 GHz measured with similar spatial resolution (Table 6). The best fit spectral index is $\alpha = 0.64_{-0.07}^{+0.06}$. Condon et al. (1982) derived a spectral index of $\alpha = 0.6$ using 1.4 and 4.85 GHz VLA measurements, while van Driel et al. (1995) derived a mean radio spectral index of $\alpha = 0.57$. The observed slope of the radio spectral index is indicative of non-thermal synchrotron radiation from optically thin supernova remnants (SNR; $\alpha \simeq 0.7$ Filho et al. 2002). However, the fact that the spectral index is a bit shallower than pure synchrotron suggests that there is a non-negligible contribution from thermal free-free emission. This scenario is supported by H92 α radio recombination line emission measurements from NGC 660, indicative of high density ionized gas (Phookun et al. 1998).

The NH_3 spectra from NGC 660 possess a high degree of structure (see Figure 3). Furthermore, although the NH_3 and H_2CO absorption features overlap in velocity, they differ in velocity width by almost an order of magnitude; $FWZI(NH_3) \simeq 150$ to 325 km s^{-1} (Table 3) and

$FWZI(H_2CO) \simeq 1000 \text{ km s}^{-1}$ (Table 2 of Mangum et al. (2013)). These facts suggest that the NH_3 and H_2CO transitions probe different spectral components of the galaxy.

Spatially resolved measurements of the nuclear region of NGC 660 make it possible to connect the NH_3 spectral components to spatial components in the galaxy. Baan et al. (1992b) have imaged the HI and OH absorption toward the nucleus of NGC 660 at $\theta_b = 1.''47$ using the VLA in its A-configuration. These observations have been supplemented with single dish observations from the Arecibo Observatory. Baan et al. (1992b) identify 12 HI absorption features and 7 distinct OH absorption features. The HI and OH absorption features have FWHM $\approx 90 \text{ km s}^{-1}$, similar to the FWHM $\sim 30 - 80 \text{ km s}^{-1}$ of our NH_3 observations. The approximately 30 km s^{-1} discrepancy between the HI/OH and NH_3 line widths can be attributed to HI and OH tracing a less dense phase of the ISM than NH_3 .

Baan et al. (1992b) place the HI features with central velocities at 675, 687, 761, 862, 965, 974, 1002, and 1018 km s^{-1} in the disk; 768, 851, and 870 km s^{-1} in the polar ring⁵; and a feature at 720 km s^{-1} in an “anomalous ridge”. Baan et al. (1992b) also place the OH features with central velocities at 675, 765, 923, 992, and 1008 km s^{-1} in the disk; one at 861 km s^{-1} in the polar ring; and one at 750 km s^{-1} in the anomalous ridge. The NH_3 absorption features presented in this work have velocity centroids between $765 - 769 \text{ km s}^{-1}$ (G1), $785 - 800 \text{ km s}^{-1}$ (G2), $828 - 839 \text{ km s}^{-1}$ (G3), and $979 - 989 \text{ km s}^{-1}$ (G4). Comparing the central velocities of our NH_3 measurements to those of Baan et al. (1992b), we place G1 and G4 in the disk and find the location of G2 to be indeterminate.

For the NH_3 G3 component, the HI observations are ambiguous with a disk component at 862 km s^{-1} and polar ring components at 851 km s^{-1} and 870 km s^{-1} . The OH observations suggest clear placement in the polar ring for G3, but keep in mind that the OH measurements of the polar ring are actually measuring the part of this component that is projected against the nucleus of the galaxy. Combes et al. (1992) have detected CO 1 - 0 emission toward two of the HI maxima (van Driel et al. 1995) identified with the polar ring component in NGC 660 at $v_{opt} = 723 - 726$ and $980 - 945 \text{ km s}^{-1}$, velocities inconsistent with our G3 component at $828 - 839 \text{ km s}^{-1}$. A more likely association of the G3 NH_3 velocity component and the narrow line K-doublet H_2CO feature at 840 km s^{-1} (Mangum et al. 2013) would place these spectral components in the nuclear region, near the nuclear starburst ring noted by Carral et al. (1990).

The HI absorption measurements point to a velocity width of $\sim 60 \text{ km s}^{-1}$ in the polar ring, much smaller than the galactic disk component, with emission line width of $\sim 350 \text{ km s}^{-1}$. Although HI is not necessarily associated with the dense gas traced by NH_3 and H_2CO , the order of magnitude difference in line width between the narrow absorption features and broad galactic emission support the interpretation of the dense NH_3 components as inhabitants of the nuclear region who are superimposed

⁵ Baan et al. (1992b) refer to the part of the polar ring component which passes in front of the nucleus as the “warp”.

directly in front of a bright, compact continuum source.

7.1. Kinetic Temperature Within the Spatial/Spectral Components of NGC 660

In Table 5 we summarize the results from our LVG model fits to the NH_3 measurements of the four velocity components which comprise NGC 660. As summarized in §7, components G1 and G4 are associated with the disk component in NGC 660, G3 is associated with the starburst ring, while the location of component G2 is indeterminate. The introduction of a background continuum source to our LVG analysis of the NH_3 absorption toward this galaxy, coupled with the detection of five non-metastable ($J \neq K$) transitions, has resulted, in many cases, to a more complex model fit.

7.1.1. Spectral Component G1

The spectral component with the lowest velocity ($v_{\text{hel}} = 767 \pm 2 \text{ km s}^{-1}$), the G1 component is only detected in the low-lying NH_3 (1,1), (2,2), and (4,4) transitions. The lower-limit kinetic temperature of $T_K \gtrsim 80 \text{ K}$ is applicable over all spatial and column densities investigated for $T_c \lesssim 300 \text{ K}$. Over more restricted ranges in spatial density and NH_3 column density of $\gtrsim 10^{6.5} \text{ cm}^{-3}$ and $\lesssim 10^{16.5} \text{ cm}^{-2}/\text{km s}^{-1}$, though, the kinetic temperature is better constrained: $T_K = 149 \pm 72 \text{ K}$ (Figure 21). As the detection of this component in only low-lying NH_3 transitions suggests a relatively low kinetic temperature, we believe that the kinetic temperature derived from this more restricted range in (n, N) better represents the true kinetic temperature of this spectral component.

7.1.2. Spectral Component G2

Detected in a total of nine NH_3 transitions (6 para, 3 ortho, 4 non-metastable), best fit cumulative and individual ratio solutions are found for $T_c \simeq 300 \text{ K}$. Apparent contributions due to multiple temperature components makes the cumulative fits using all para- NH_3 (both metastable and non-metastable) transitions poor. Individual ratio fits to our (2,2)/(4,4) and (4,4)/(5,5) para- NH_3 measurements yields $T_K \gtrsim 40 \text{ K}$ and $\gtrsim 220 \text{ K}$, respectively.

As the non-metastable transitions can be affected by infrared excitation, we have performed cumulative LVG model fits constrained by our para- NH_3 metastable ($J=K$) transitions. These fits produce a lower-limit $T_K \gtrsim 260 \text{ K}$ over a limited range in (n, N) of $\lesssim 10^{5.0} \text{ cm}^{-3}$ and $\gtrsim 10^{16.5} \text{ cm}^{-2}/\text{km s}^{-1}$, respectively. Finally, LVG model fits to our metastable ortho- NH_3 (3,3)/(6,6) measurements yield a rather poorly-constrained $T_K = 173 \pm 106 \text{ K}$ for a limited range in (n, N) of $\gtrsim 10^{6.0} \text{ cm}^{-3}$ and $\gtrsim 10^{16.5} \text{ cm}^{-2}/\text{km s}^{-1}$, respectively. These LVG model fits, taken with the detection of the high-excitation (5,5) and (6,6) transitions, suggest that a good lower-limit to the kinetic temperature of the G2 component is 150 K .

7.1.3. Spectral Component G3

As with G1 and G2, cumulative best fit solutions assuming $T_c \simeq 300 \text{ K}$, are all rather poor. As was done with the G2 spectral component, using only metastable para- NH_3 transitions in our LVG model fit resulted in only slight improvement, suggesting that $T_K \gtrsim 100 \text{ K}$. Looking at fits to individual ratios:

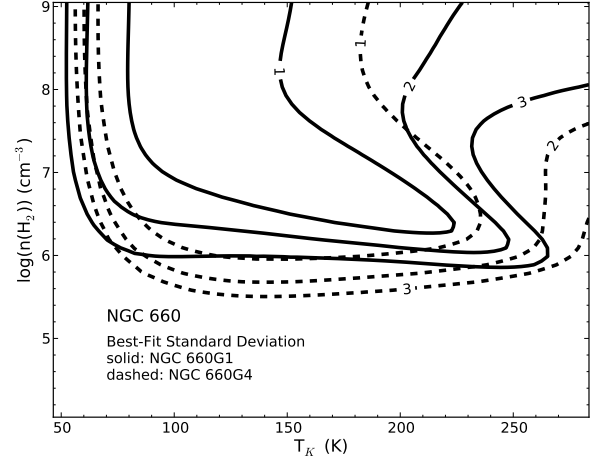


FIG. 21.— NH_3 LVG model best-fit kinetic temperature toward the G1 and G4 spectral components of NGC 660 at the representative $N(\text{para-NH}_3)/\Delta v = 10^{16.5} \text{ cm}^{-2}/\text{km s}^{-1}$. Shown are the metastable para- NH_3 best-fit 1, 2, and 3σ standard deviation to NGC 660G1 (solid) and G4 (dashed) assuming a background continuum temperature of 300 K .

- (1,1)/(2,2): $T_K = 154 \pm 96 \text{ K}$
- (2,2)/(4,4): $T_K \gtrsim 68 \text{ K}$
- (3,3)/(6,6): $T_K = 179 \pm 121 \text{ K}$
- (4,4)/(5,5): $T_K \gtrsim 200 \text{ K}$
- (5,5)/(7,7): $T_K \gtrsim 284 \text{ K}$ for $N \lesssim 10^{14.5} \text{ cm}^{-2}/\text{km s}^{-1}$ and $T_K \gtrsim 88 \text{ K}$ for $(n, N) \gtrsim (10^{6.5} \text{ cm}^{-3}, 10^{14.5} \text{ cm}^{-2}/\text{km s}^{-1})$.

As noted with the analysis of our ortho- NH_3 measurements of NGC 3079, one should be cautious with fits to the (3,3) and (6,6) transitions as slight differences in the spatial and column densities and kinetic temperatures at which the (3,3) and (6,6) transitions produce emission and absorption corrupt the uniqueness of their kinetic temperature sensitivity. This results in a “double-value” to the best-fit kinetic temperature for $n(\text{H}_2) > 10^{4.5} \text{ cm}^{-3}$. The kinetic temperature range indicated includes the limits of this double-value fit. The kinetic temperature for the G3 spectral component appears to be $\gtrsim 100 \text{ K}$.

7.1.4. Spectral Component G4

Best-fit solutions constrained by all para- NH_3 transitions are surprisingly good, yielding $T_K = 174 \pm 82 \text{ K}$. Constraining only the metastable para- NH_3 transitions results in a fit to the kinetic temperature of $T_K = 149 \pm 84 \text{ K}$ for $n(\text{H}_2) \gtrsim 10^6 \text{ cm}^{-3}$ and $N(\text{para-NH}_3)/\Delta v < 10^{16.75} \text{ cm}^{-2}/\text{km s}^{-1}$ (Figure 21). For the LVG model fit using only the metastable ortho- NH_3 (3,3)/(6,6) ratio we derive $T_K = 160 \pm 90 \text{ K}$. Taking all three kinetic temperature measurements together we estimate $T_K = 163 \pm 93 \text{ K}$ for the G4 spectral component.

7.2. NGC 660 Spectral Component Summary

Table 7 summarizes the NH_3 spectral components, their association with spatially-identified HI and/or OH

spectral components, and their derived kinetic temperatures. Our NH_3 measurements suggest that both the disk and starburst ring components harbor dense, high kinetic temperature gas.

8. SPATIAL EXTENT OF THE NH_3 EMITTING GAS

An estimate to the size of the NH_3 emitting region within each of the galaxies in our sample can be derived from the measured NH_3 transition intensities ($T_{mb} = \frac{T_A^*}{\eta_{mb}}$), an estimate of the optical depth (τ), our derived kinetic temperatures ($T_{rot} = T_K$), and the radiative transfer equation in a uniform medium:

$$\begin{aligned} T_{mb} &= f T_{rot} (1 - \exp(-\tau)) \\ \frac{T_A^*}{\eta_{mb}} &\simeq f T_K \tau \\ f &\simeq \frac{T_A^*}{\eta_{mb} \tau T_K} \end{aligned} \quad (4)$$

where f is the areal filling factor of the NH_3 emission in our primary beam ($\theta_b \simeq 30''$). In Equation 4 we have assumed that all measured transitions are optically thin ($\tau \ll 1$) and that the NH_3 rotation temperature (T_{rot}) is equal to the kinetic temperature in the gas (T_K). Measured T_A^* values are listed in Table 3, derived T_K values are given in Table 5, and $\eta_{mb} = 0.87$ (§3). NH_3 transition optical depths can be derived from our LVG models, but since the optical depth for a given transition is dependent upon the intensity of that transition, which is, as Equation 4 shows, dependent upon the areal filling factor f , we only have an upper limit to τ at our disposal. For non-masing (para- NH_3) transitions $\tau \lesssim 0.1$ with only a minor dependence on spatial density. Note too that for galaxies with lower limits to their dense gas kinetic temperatures, coupled to the upper limit to τ , that f is indeterminate. With these limitations in mind, and using the measured T_A^* , τ , and T_K (excluding lower limit values) values for our NH_3 measurements, we derive the lower-limits to the areal filling factor f listed in Table 8. As the areal filling factor f is related to the source emission extent (θ_s or d_s) and the measurement beam size (θ_b or d_b):

$$\begin{aligned} f &= \left(\frac{\theta_s}{\theta_b} \right)^2 \\ &= \left(\frac{d_s}{d_b} \right)^2 \end{aligned} \quad (5)$$

and our GBT primary beam diameter $\theta_b = 30''$ has a physical size (d_b) of 290 pc at a distance of 1 Mpc, we can derive lower-limits to the physical size of the NH_3 emitting regions (d_s ; Table 8). The lower limits to d_s derived correspond to the analogs of molecular and giant molecular clouds in our own Galaxy.

9. HOW CAN GALAXIES SUPPORT SUCH HIGH KINETIC TEMPERATURES?

With few exceptions the kinetic temperatures we derive range from 50 to > 250 K. The physical size scales over which our $\theta_b \simeq 30''$ NH_3 measurements are sensitive range from ~ 10 pc to ~ 30 kpc (§8). As these physical

size scales are potentially quite large, one has to wonder how such high kinetic temperatures can be maintained in these regions.

The dense gas environments and high star formation rates in star forming galaxies have been modelled by several groups using adaptations of chemical Photon Dominated Region (PDR) models which incorporate cosmic ray (CR; Bayet et al. 2011), CR plus UV, X-ray, and mechanical (Loenen et al. 2008), and CR plus mechanical (Meijerink et al. 2011, Meijerink, R., private communication) heating. These models predict $T_K = 30 - 500$ K, with higher kinetic temperatures corresponding to higher CR and/or mechanical heating rates. For reference, star formation rates (SFR in M_\odot/yr), supernova rates (SNR per year), and mechanical heating rates (Γ_{mech} in $\text{erg cm}^{-2} \text{s}^{-1}$) correspond to (1, 0.01, 2×10^{-20}) for disks of quiescent galaxies (i.e. the Milky Way), (50, 0.3, 1×10^{-18}) for star formation regions, and (1000, 6.4, 2×10^{-18}) for extreme starbursts (Kazandjian et al. 2012). This suggests that an active star formation process in galaxies can generate the necessary mechanical heating input that is required to in-turn generate the high kinetic temperatures measured in galaxies with high star formation rates.

In the CR plus mechanical heating models of Meijerink et al. (2011), $T_K \simeq 100 - 200$ K for a mechanical heating rate of $3 \times 10^{-18} \text{ erg cm}^{-2} \text{s}^{-1}$ in a high density ($n(\text{H}_2) = 10^{5.5} \text{ cm}^{-3}$) high column density ($N(\text{H}_2) > 10^{22} \text{ cm}^{-2}$) environment with CR rates ranging from $5 \times 10^{-17} - 5 \times 10^{-14} \text{ s}^{-1}$. In the Bayet et al. (2011) models which include only CR heating the NH_3 abundance declines rapidly with increasing CR rate. In contrast, the modified PDR models of Meijerink et al. (2011) predict that the addition of mechanical heating with energy density $\Gamma = 2 \times 10^{-17} \text{ erg cm}^{-3} \text{s}^{-1}$ will result in an order-of-magnitude increase in the NH_3 abundance at the highest column densities ($N(\text{H}_2) \simeq 3 \times 10^{22} \text{ cm}^{-2}$) and a CR rate of $5 \times 10^{-14} \text{ s}^{-1}$. We should also point out that a similar heating scenario, involving cosmic ray and/or turbulent energy dissipation (mechanical) heating, is suggested based on measurements of the dense molecular clouds in the central molecular zone (CMZ) of our Galaxy (Ao et al. 2013). It appears then that the high kinetic temperatures that we derive for the dense star formation regions in our galaxy sample, and in the CMZ of our own Galaxy, can be produced by both cosmic ray and mechanical heating processes.

To investigate how the high kinetic temperatures we measure might manifest themselves as traditional star formation indicators, we have investigated the correlation between our measured gas kinetic temperatures and star formation rate, as indicated by infrared luminosity (L_{IR}) or radio flux at 5 GHz. Kinetic temperature is uncorrelated to either of these quantities. We have also looked for correlation between T_K and the relative proportion of dust emission at $12 \mu\text{m}$, $25 \mu\text{m}$, and $60 \mu\text{m}$, again finding no correlation. This lack of correlation with global star formation indicators suggests that the high kinetic temperatures we measure are associated with more localized processes. Unfortunately, physical processes that are more localized in nature and that are also associated with star formation, including shocks, outflows, or merger state, are not well character-

TABLE 7
NGC 660 SPECTRAL/SPATIAL COMPONENT CORRESPONDENCE

Component	$v_{hel}(\text{NH}_3)$ (km s ⁻¹)	$v_{hel}(\text{OH})$ (km s ⁻¹)	$v_{hel}(\text{HI})$ (km s ⁻¹)	Spatial Assoc	T_K (K)
G1	765–769	765	761	disk	149 ± 72
G2	785–800	indeterminate	≥ 150
G3	828–839	861	851,862,870	starburst ring	≥ 100
G4	970–989	992,1008	965,974,1002	disk	163 ± 93

TABLE 8
GALAXY AMMONIA AREAL FILLING FACTOR LIMITS

Galaxy	d_b^a (pc)	f	d_s (pc)
NGC 253	998	~ 0.01	~ 100
NGC 660	3538	~ 0.01	~ 354
NGC 891 ^b	2734	~ 0.0002	~ 38
Maffei 2	902	~ 0.001	~ 10
NGC 1365	6236	~ 0.001	~ 62
IC 342	1108	~ 0.01	~ 110
M 82SW	1716	~ 0.001	~ 18
NGC 3079 ^c	6004
M 83	1168	~ 0.001	~ 12
IC 860	15602	~ 0.001	~ 156
IR 15107+0724	17952	~ 0.001	~ 180
Arp 220	24042	~ 0.001	~ 240
NGC 6946	1592	~ 0.001	~ 16

^a Using the angular size distance $D_A = \frac{D_L}{(1+z)^2}$ with D_L from Table 2.

^b The extremely low lower-limit for f and d_s for NGC 891 is due to the very low upper-limit to T_K of < 30 K for this galaxy.

^c As all T_K derived for NGC 3079 are lower-limits, f and d_s are indeterminant.

ized in our galaxy sample.

A quantification of the spatial distribution of the dense hot gas we measure within the galaxies in our sample would certainly shed some light on the exact physical process that is producing the high kinetic temperatures we measure. NH_3 enhancement has been associated with shock excitation in outflows (i.e. L1157: Umemoto et al. (1992); Tafalla & Bachiller (1995); Viti et al. (2011)) within our Galaxy, allowing for the possibility that the actual distribution of dense hot gas we measure is actually tracing the interfaces between shocks and dense molecular clouds. As noted above, the mechanical heating rates implied by star formation and starbursts are consistent with dense gas at $T_K \simeq 100 - 200$ K. A plausible model of the spatial distribution of this dense hot gas would suggest that it emanates from numerous active star formation regions that are concentrated within the dense gas components, primarily nuclei, of the galaxies in our sample. One could envision this as a “plum pudding” model whereby the hot gas we measure traces compact knots of active star formation within a more extended, yet still dense, star-forming environment.

10. WHY ARE DUST TEMPERATURES A POOR PROXY FOR GAS TEMPERATURES?

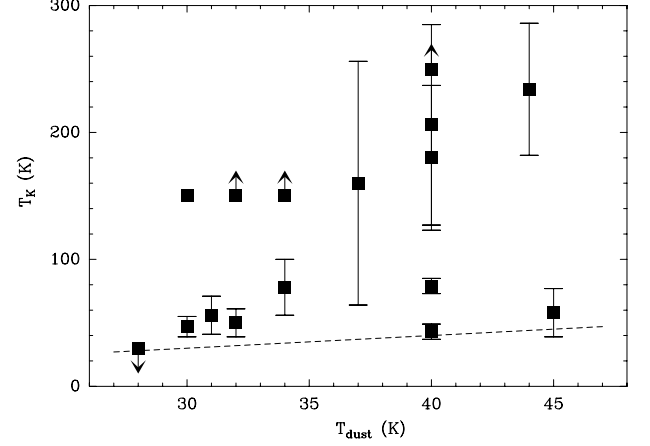


FIG. 22.— Galaxy sample dust temperature (T_{dust}) versus kinetic temperature (T_K). For the kinetic temperature values we have used the “whole galaxy” values listed in Table 5. The dashed line represents $T_{dust} = T_K$.

Related to the issue of the high kinetic temperatures in our star forming galaxy sample is the use of dust temperatures as a proxy for gas kinetic temperatures in these galaxies. As noted in Mangum et al. (2013), the common practice of using the dust temperature derived from IRAS 60 and $100 \mu\text{m}$ fluxes as a proxy for gas kinetic temperature was applied to the star forming galaxy sample presented in Mangum et al. (2008). Table 5 lists the dust and gas kinetic temperatures derived for all of the galaxies in our sample, while Figure 22 displays these temperatures. While dust temperatures range from 28 to 45 K, NH_3 -based gas kinetic temperatures range from ~ 25 to > 250 K, with no apparent correlation between T_{dust} and T_K (Figure 22). Clearly the assumption that $T_{dust} = T_K$ is not correct.

Issues with the veracity of the application of dust temperatures as a proxy for kinetic temperatures have been noted before. Helou (1986) noted that dust emission at 12 and $25 \mu\text{m}$ traces primarily active star formation while 60 and $100 \mu\text{m}$ emission traces cooler “cirrus” emission from ambient dust heated by existing stellar populations. A similar analysis of *Spitzer* Space Telescope and *Herschel* Space Observatory measurements of the dust emission from M 81, M 83, and NGC 2403 (Bendo et al. 2012) concluded that dust emission at wavelengths less than $160 \mu\text{m}$ generally originates from active star formation regions, while dust emission at wavelengths greater than

250 μm originates primarily from colder dust components which are relatively unassociated with star formation activity. A similar *Herschel* Space Observatory study of the dust continuum emission from M31 (Groves et al. 2012) found that the heating source for the submillimeter dust emission from this galaxy originates in the older ($\gtrsim 10^9$ years) stellar populations that inhabit the bulge of M31. It appears then that longer-wavelength infrared measurements do not trace active star formation in galaxies, and that long-wavelength infrared measurements should not be used as a proxy for dust and gas kinetic temperatures in such regions.

Nowhere is this discrepancy between dust and gas kinetic temperatures more apparent than in our own Galactic center. Ao et al. (2013) used para- H_2CO $3_{03} - 2_{02}$, $3_{22} - 2_{21}$, and $3_{21} - 2_{20}$ measurements of the Galactic plane and the Galactic center to measure the kinetic temperature of the dense molecular clouds in these regions over spatial scales of 1.2 pc. Ao et al. (2013) found that T_K ranged from 50 to > 100 K in the Galactic center, with the molecular clouds possessing the highest kinetic temperatures located closest to the Galactic center. These H_2CO -derived gas kinetic temperatures are much higher than the fairly uniform dust temperatures of $\sim 14 - 20$ K measured toward the dense molecular clouds of the Galactic center (Pierce-Price et al. 2000; García-Marín et al. 2011; Molinari et al. 2011). Ao et al. (2013) argue that the high gas kinetic temperatures measured may be caused by turbulent and/or cosmic-ray heating, but cannot be caused by photon (irradiative) processes.

11. CONCLUSIONS

We have used measurements of 15 NH_3 transitions to derive the kinetic temperature in a sample of 23 star forming low-redshift galaxies and one galaxy offset position. A summary of our conclusions are:

- Of the 23 galaxies and one galaxy offset position measured, we detect at least one NH_3 transition toward 13 of these galaxies.
- Using our NH_3 measurements to derive the kinetic temperature, we find that 9 of the 13 galaxies possess multiple kinetic temperature and/or velocity components.
- The kinetic temperatures derived toward our galaxy sample are in many cases at least a factor of two larger than kinetic temperatures derived previously from mainly lower-excitation NH_3 measurements.
- The derived kinetic temperatures in our galaxy sample, which are in many cases at least a factor of two larger than derived dust temperatures, point to a problem with the common assumption that dust and gas kinetic temperatures are equivalent. As previously suggested, the use of dust emission at wavelengths greater than 160 μm to derive dust temperatures, or dust heating from older stellar populations, may be skewing derived dust temperatures in these galaxies to lower values.
- The non-metastable NH_3 (2,1) transition has been detected toward 4 galaxies: two in emission and

two absorption. Non-metastable NH_3 (3,1), (3,2), (4,3), (5,4) (toward NGC 660) and (10,9) (toward Arp 220) have also been detected, all in absorption.

- The polar ring galaxy NGC 660 possesses the most remarkably complex NH_3 absorption profile in our sample.
 - The NH_3 and H_2CO spectral components from this galaxy overlap in velocity but differ by almost an order-of-magnitude in velocity width ($\text{FWZI}(\text{NH}_3) \simeq 150$ to 325 km s^{-1} ; $\text{FWZI}(\text{H}_2\text{CO}) \simeq 1000 \text{ km s}^{-1}$). This suggests that NH_3 traces a more quiescent environment in the star formation regions of NGC 660 than that traced by H_2CO . NGC 660 is the only galaxy which shows this disparity between NH_3 and H_2CO spectral component widths.
 - The four NH_3 velocity components which comprise NGC 660 have been associated with previously-measured disk, and possibly ring, components.
 - Derived kinetic temperatures within the four spectral components of NGC 660 range from > 100 to 163 ± 93 K.
- As originally shown by Mangum & Wootten (1994) for the ortho- NH_3 (3,3) transition, the ortho- NH_3 (3,3) and (6,6) transitions mase over a wide range of physical conditions. As our LVG models include a proper treatment of the collisional excitation process which leads to maser emission in these transitions, the NH_3 $\frac{(3,3)}{(6,6)}$ ratio is a viable probe of the kinetic temperature when properly modelled.
- Unlike all other galaxies in our NH_3 sample which exhibit high-excitation NH_3 (6,6) (and in the case of NGC 253, NH_3 (9,9)) emission, we do not detect the NH_3 (3,3) transition toward NGC 3079. As the lower-excitation ortho- NH_3 transitions can be excited into maser emission states under a variety of conditions, a two-spatial component model which includes overlapping NH_3 (3,3) emission and absorption components can explain this lack of NH_3 (3,3) emission or absorption. This physical scenario is supported by the complex emission and absorption observed in H_2CO $1_{10} - 1_{11}$ (Mangum et al. 2008, 2013).
- The merger system Arp 220, in addition to possessing high kinetic temperatures within its two velocity component structure, exhibits unusually broad NH_3 (2,2) and comparatively narrow and weak NH_3 (1,1) absorption. This unusual NH_3 (1,1) and (2,2) spectral structure has been previously explained (Ott et al. 2011) as due to an overlapping cold ($T_K \lesssim 20$ K) component. An alternative explanation which appears to be consistent with our NH_3 measurements is that there is a broad velocity component shifted by approximately $\sim 200 \text{ km s}^{-1}$ relative to the nominal velocity components in Arp 220 which modifies the relative widths and intensities of the NH_3 (1,1) and (2,2) transitions. This scenario is supported by the

measurement of a similar broad velocity component in the *Herschel*/PACS spectra of OH, [OI], and H₂O (González-Alfonso et al. 2012).

- We confirm the tentative detection of OH $^2\Pi_{3/2}$ J=9/2 absorption toward Arp 220 by Ott et al. (2011). This confirmation is consistent with far infrared high-excitation OH $^2\Pi_{1/2}$ and $^2\Pi_{3/2}$ absorption measurements toward Arp 220 (González-Alfonso et al. 2012). A significant contributor to this high-excitation OH absorption appears to originate from a dense outflow component in Arp 220.

The GBT staff, especially Frank Ghigo, were characteristically helpful and contributed significantly to the

success of our observing program. Our anonymous referee provided very useful suggestions which improved the quality of this work. JGM thanks Rowin Meijerink for providing calculations of NH₃ and H₂CO abundance from his chemical models. JGM also thanks Brian Kent, who was instrumental in providing the python script that was used to extrapolate the NH₃ collisional excitation rates. Support for this work was provided by NASA through Hubble Fellowship grant #HST-HF-01183.01-A awarded by the Space Telescope Science Institute, which is operated by the Association of Universities for Research in Astronomy, Incorporated, under NASA contract NAS5-26555. This research has made use of the NASA/IPAC Extragalactic Database (NED) which is operated by the Jet Propulsion Laboratory, California Institute of Technology, under contract with the National Aeronautics and Space Administration.

Facilities: GBT

REFERENCES

- Aalto, S., García-Burillo, S., Muller, S., et al. 2012, *A&A*, 537, A44
- Anantharamaiah, K. R., Viallefond, F., Mohan, N. R., Goss, W. M., & Zhao, J. H. 2000, *ApJ*, 537, 613
- Ao, Y., Henkel, C., Menten, K. M., et al. 2013, *A&A*, 550, A135
- Baan, W. A., Haschick, A., & Henkel, C. 1992a, *AJ*, 103, 728
- Baan, W. A., Rhoads, J., & Haschick, A. D. 1992b, *ApJ*, 401, 508
- Bayet, E., Williams, D. A., Hartquist, T. W., & Viti, S. 2011, *MNRAS*, 414, 1583
- Becker, R. H., White, R. L., & Edwards, A. L. 1991, *ApJS*, 75, 1
- Bendo, G. J., Boselli, A., Dariush, A., et al. 2012, *MNRAS*, 419, 1833
- Carral, P., Turner, J. L., & Ho, P. T. P. 1990, *ApJ*, 362, 434
- Chini, R., & Kruegel, E. 1993, *A&A*, 279, 385
- Combes, F., Braine, J., Casoli, F., Gerin, M., & van Driel, W. 1992, *A&A*, 259, L65
- Condon, J. J. 1980, *ApJ*, 242, 894
- Condon, J. J., Condon, M. A., Gisler, G., & Puschell, J. J. 1982, *ApJ*, 252, 102
- Condon, J. J., Helou, G., Sanders, D. B., & Soifer, B. T. 1990, *ApJS*, 73, 359
- Danby, G., Flower, D. R., Valiron, P., et al. 1987, *Journal of Physics B: Atomic and Molecular Physics*, 20, 1039
- Danby, G., Flower, D. R., Valiron, P., Schilke, P., & Walmsley, C. M. 1988, *MNRAS*, 235, 229
- Downes, D., Radford, S. J. E., Guilleoteau, S., et al. 1992, *A&A*, 262, 424
- Dressel, L. L., & Condon, J. J. 1978, *ApJS*, 36, 53
- Dudik, R. P., Satyapal, S., Gliozzi, M., & Sambruna, R. M. 2005, *ApJ*, 620, 113
- Duric, N., Seaquist, E. R., Crane, P. C., Bignell, R. C., & Davis, L. E. 1983, *ApJ*, 273, L11
- Filho, M. E., Barthel, P. D., & Ho, L. C. 2002, *ApJS*, 142, 223
- Flower, D. R., Pineau des Forets, G., & Walmsley, C. M. 1995, *A&A*, 294, 815
- Gao, Y., & Solomon, P. M. 2004a, *ApJS*, 152, 63
- . 2004b, *ApJ*, 606, 271
- García-Marín, M., Eckart, A., Weiss, A., et al. 2011, *ApJ*, 738, 158
- González-Alfonso, E., Fischer, J., Graciá-Carpio, J., et al. 2012, *A&A*, 541, A4
- Gregory, P. C., & Condon, J. J. 1991, *ApJS*, 75, 1011
- Greve, T. R., Papadopoulos, P. P., Gao, Y., & Radford, S. J. E. 2009, *ApJ*, 692, 1432
- Groves, B., Krause, O., Sandstrom, K., et al. 2012, *MNRAS*, 426, 892
- Heckman, T. M., Lehnert, M. D., Strickland, D. K., & Armus, L. 2000, *ApJS*, 129, 493
- Helou, G. 1986, *ApJ*, 311, L33
- Henkel, C., Baan, W. A., & Mauersberger, R. 1991, *A&A Rev.*, 3, 47
- Henkel, C., Mauersberger, R., Peck, A. B., Falcke, H., & Hagiwara, Y. 2000, *A&A*, 361, L45
- Hermesen, W., Wilson, T. L., Walmsley, C. M., & Henkel, C. 1988, *A&A*, 201, 285
- Kazandjian, M. V., Meijerink, R., Pelupessy, I., Israel, F. P., & Spaans, M. 2012, *A&A*, 542, A65
- Kukula, M. J., Pedlar, A., Baum, S. A., & O'Dea, C. P. 1995, *MNRAS*, 276, 1262
- Large, M. I., Mills, B. Y., Little, A. G., Crawford, D. F., & Sutton, J. M. 1981, *MNRAS*, 194, 693
- Lebrón, M., Mangum, J. G., Mauersberger, R., et al. 2011, *A&A*, 534, A56
- Lindberg, J. E., Aalto, S., Costagliola, F., et al. 2011, *A&A*, 527, A150
- Loenen, A. F., Spaans, M., Baan, W. A., & Meijerink, R. 2008, *A&A*, 488, L5
- Mangum, J. G., Darling, J., Henkel, C., & Menten, K. M. 2013, *ApJ*, 766, 108
- Mangum, J. G., Darling, J., Menten, K. M., & Henkel, C. 2008, *ApJ*, 673, 832
- Mangum, J. G., & Wootten, A. 1993, *ApJS*, 89, 123
- . 1994, *ApJ*, 428, L33
- Martin, R. N., & Ho, P. T. P. 1979, *A&A*, 74, L7
- Mauersberger, R., Henkel, C., Weiß, A., Peck, A. B., & Hagiwara, Y. 2003, *A&A*, 403, 561
- Meier, D. S., & Turner, J. L. 2001, *ApJ*, 551, 687
- . 2005, *ApJ*, 618, 259
- Meier, D. S., Turner, J. L., & Schinnerer, E. 2011, *AJ*, 142, 32
- Meijerink, R., Spaans, M., Loenen, A. F., & van der Werf, P. P. 2011, *A&A*, 525, A119
- Molinari, S., Bally, J., Noriega-Crespo, A., et al. 2011, *ApJ*, 735, L33
- Montero-Castaño, M., Herrnstein, R. M., & Ho, P. T. P. 2006, *ApJ*, 646, 919
- Morris, M., Zuckerman, B., Palmer, P., & Turner, B. E. 1973, *ApJ*, 186, 501
- Nguyen, Q.-R., Jackson, J. M., Henkel, C., Truong, B., & Mauersberger, R. 1992, *ApJ*, 399, 521
- Ott, J., Henkel, C., Braatz, J. A., & Weiß, A. 2011, *ApJ*, 742, 95
- Ott, J., Weiss, A., Henkel, C., & Walter, F. 2005, *ApJ*, 629, 767
- Ott, M., Witzel, A., Quirrenbach, A., et al. 1994, *A&A*, 284, 331
- Phookun, B., Anantharamaiah, K. R., & Goss, W. M. 1998, *MNRAS*, 295, 156
- Pierce-Price, D., Richer, J. S., Greaves, J. S., et al. 2000, *ApJ*, 545, L121
- Salter, C. J., Ghosh, T., Catinella, B., et al. 2008, *AJ*, 136, 389
- Sanders, D. B., Mazzarella, J. M., Kim, D.-C., Surace, J. A., & Soifer, B. T. 2003, *AJ*, 126, 1607
- Sobolev, V. V. 1960, *Moving Envelopes of Stars* (Cambridge: Harvard University Press, 1960)
- Sramek, R. 1975, *AJ*, 80, 771
- Tafalla, M., & Bachiller, R. 1995, *ApJ*, 443, L37
- Takano, S., Hofner, P., Winniewisser, G., Nakai, N., & Kawaguchi, K. 2005, *PASJ*, 57, 549
- Takano, S., Nakai, N., & Kawaguchi, K. 2002, *PASJ*, 54, 195
- Takano, S., Nakai, N., Kawaguchi, K., & Takano, T. 2000, *PASJ*, 52, L67
- Umamoto, T., Iwata, T., Fukui, Y., et al. 1992, *ApJ*, 392, L83
- van Driel, W., Combes, F., Casoli, F., et al. 1995, *AJ*, 109, 942
- Viti, S., Jimenez-Serra, I., Yates, J. A., et al. 2011, *ApJ*, 740, L3
- Walmsley, C. M., & Ungerechts, H. 1983, *A&A*, 122, 164
- Weiß, A., Neining, N., Henkel, C., Stutzki, J., & Klein, U. 2001, *ApJ*, 554, L143
- Young, J. S., & Scoville, N. Z. 1991, *ARA&A*, 29, 581